

A parametric study of population inversions in relativistic plasmas through nonresonant interactions with Alfvén waves and their applications to Fast Radio Bursts

Killian Long,^{1*} Asaf Pe’er,²

¹*Department of Physics, University College Cork, Cork, Ireland*

²*Bar-Ilan University, Ramat-Gan 5290002, Israel*

Accepted XXX. Received YYY; in original form ZZZ

ABSTRACT

Synchrotron maser emission is a leading candidate to explain the coherent emission from Fast Radio Bursts (FRBs). This mechanism requires a population inversion in order to operate. We show that nonresonant interactions between Alfvén waves and a relativistic plasma result in the formation of population inversions across a wide range of magnetizations, $\sigma \gtrsim 10^{-4}$, and temperatures, $10^{-2} \leq k_b T / mc^2 \leq 3$, spanning the parameters expected in FRB environments. We calculate the fraction of energy contained in the inversion across the whole of this parameter space for the first time and we show that energy fractions of $f_{inv} \sim 0.3$ are achieved for high magnetizations $\sigma > 1$. The population inversion forms on time-scales compatible with the typical dynamical time-scales of magnetars for all magnetizations. Furthermore, we provide physical explanations for the behaviour of the interaction in different magnetization regimes, and identify the important characteristic values at which this behaviour changes. We also show that the mechanism is capable of producing an FRB signal at GHz frequencies in a relativistic magnetar wind close to the light cylinder and that this signal can escape the magnetar environment without significant damping.

Key words: fast radio bursts – plasmas – stars:magnetars

1 INTRODUCTION

The identity of the emission mechanism responsible for Fast Radio Bursts (FRBs) is an open question, prompting the development of numerous theories (for a summary, see [Platts et al. 2019](#)). All models share the need to explain the extremely high FRB brightness temperatures of up to $T_b \sim 10^{36}$ K (e.g. [Katz 2016](#)), far in excess of those achievable by incoherent radiation. One of the primary coherent emission mechanisms invoked to explain the observed FRB signal is synchrotron maser emission (SME) (e.g. [Lyubarsky 2014](#); [Long & Pe’er 2018](#); [Metzger et al. 2019](#)).

The synchrotron maser, or its mildly relativistic equivalent the cyclotron maser, is a proposed emission mechanism not only for FRBs, but for many other coherent astrophysical phenomena such as Auroral Kilometric Radiation (AKR) in the Earth’s magnetosphere ([Wu & Lee 1979](#); [Wu 1985](#)), Jovian Decametric Radiation (e.g. [Hewitt et al. 1982](#)), and blazars ([Begelman et al. 2005](#)). SME requires a certain set of plasma conditions: (i) an inverse population of energetic electrons, and (ii) a background magnetic field. Once these conditions are satisfied, the interaction between the inverse electron population and electromagnetic waves in the plasma results in negative absorption and stimulated emission for certain plasma parameters ([Wu 1985](#); [Treumann 2006](#)).

To achieve the necessary population inversion, the particle distribution must either grow faster than E^2 ([Sagiv & Waxman 2002](#)), or satisfy $\frac{\partial F}{\partial v_{\perp}} > 0$ ([Wu 1985](#)). Here, $F(v_{\perp}, v_{\parallel})$ is the particle distribution function, v_{\perp} (v_{\parallel}) is the velocity perpendicular (parallel) to the background magnetic field, and E is the particle’s energy. The mechanism by which this population inversion forms is crucial to understanding the parameter space where SME is a viable emission mechanism. Various processes have been proposed to pump the electrons into the inverse population. Many of these models, such as the ‘loss-cone’ ([Wu 1985](#); [Freund & Wu 1976](#)) and ‘ring-shell’ ([Pritchett & Strangeway 1985](#); [Winglee & Dulk 1986](#)) models were developed for non- or mildly relativistic scenarios such as AKR.

In the context of FRBs, the environment may be relativistic with temperatures of $k_B T \approx m_e c^2$ (e.g. [Babul & Sironi 2020](#); [Beloborodov 2020](#)). Here, k_B is the Boltzmann constant, m_e is the electron mass and c is the speed of light in vacuum. In a previous work ([Long & Pe’er 2023](#)), we showed that nonresonant interactions between Alfvén waves and a plasma can produce a population inversion capable of supporting SME with a high efficiency, even in such relativistic plasmas. This mechanism does not require a shock wave as in the other primary models for relativistic SME, where a soliton-like structure is formed at the front of a strongly magnetized shock in which particles gyrate around the enhanced magnetic field and form a semi-coherent ring in momentum space (e.g. [Al-](#)

* E-mail: killian.long@umail.ucc.ie (KL)

sop & Arons 1988; Gallant et al. 1992; Amato & Arons 2006; Plotnikov & Sironi 2019). Similar ring distributions may also be formed through radiation reaction cooling (Bilbao & Silva 2023; Bilbao et al. 2024b,a).

Nonresonant interactions between the Alfvén waves and the relativistic plasma induce pitch-angle diffusion in low β plasmas, where β is the ratio of the plasma pressure to the magnetic pressure. In the emission regions of FRBs the environment is highly magnetized, satisfying this condition even at relativistic temperatures. The resulting deformation of the initial particle distribution into a crescent shape in momentum space is capable of supporting a population inversion (Zhao & Wu 2013; Wu et al. 2014).

In this work, we build upon the proof of concept results presented in Long & Pe'er (2023) where the full relativistic interaction was studied for the first time. We explore the details of the fraction of the distribution's energy contained in the population inversion as well as the time-scales required. We examine a large parameter space in both temperature T and magnetization $\sigma = \Omega^2/\omega_p^2$ for the first time. Here $\Omega = eB_0/mc$ is the gyration frequency of the plasma as a whole and $\omega_p = \sqrt{4\pi ne^2/m}$ is the plasma frequency, e is the electron charge, B_0 is the background magnetic field, and n is the particle number density. The entire magnetization parameter space $\sigma > 10^{-4}$ is investigated at temperatures in the range $10^{-2} \leq \theta \leq 3$, where $\theta = \frac{k_B T}{mc^2}$ is the normalized temperature, providing a full picture of the interaction across all the relevant physical parameters.

As in Long & Pe'er (2023), to examine the problem we consider a relativistic plasma of density n embedded in a background magnetic field \mathbf{B}_0 . The initial particle distribution $F_0(p_{\parallel}, p_{\perp}, \theta_0)$ is taken to be a Maxwell-Jüttner distribution with temperature θ_0 , where $p_{\perp} = \gamma m v_{\perp}$ and $p_{\parallel} = \gamma m v_{\parallel}$ are the relativistic momenta in the perpendicular and parallel directions to the background magnetic field respectively. Here, $\gamma = (1 + (p_{\perp}/mc)^2 + (p_{\parallel}/mc)^2)^{1/2}$ is the Lorentz factor. The nonresonant interaction between the particles and the waves causes the distribution to evolve, with the details of the development depending on the magnetization and temperature. This evolved distribution is specified at time t by $F(p_{\parallel}, p_{\perp}, t)$. In order for nonresonant interactions to occur, it is necessary for Alfvén waves to propagate through the plasma in addition to the steady background magnetic field. In the typical FRB scenario, the Alfvén waves are generated by a central neutron star/magnetar, resulting in a wavevector that is expected to be in the parallel direction only. The spectral magnetic and electric fields of the waves are denoted as B_k and E_k respectively, where k is the wavenumber. The waves are assumed to vary slowly in time, and to have a broad spectrum (Wu & Yoon 2007; Yoon et al. 2009).

This paper is organized as follows. In Section 2 we detail the physical setup of our model and the equations which describe it. The behaviour of the full relativistic quasilinear kinetic equation for different parameters and the numerical methods used to solve the equation are examined in Section 3, with some semi-analytical results for the behaviour of individual terms derived in Appendix A. In Section 4 we present the results for both the energy fraction contained in the population inversion and the relevant formation time-scales. These results are discussed and compared to the physical conditions necessary to produce FRBs in Section 5, and the results of the paper are summarized in the conclusion in Section 6.

2 NON-RESONANT INTERACTION OF PARTICLES WITH ALFVÉN WAVES: EVOLUTION OF THE PARTICLE DISTRIBUTION FUNCTION

We use kinetic theory to study the interaction between the waves and particles. The quasilinear approximation of this theory (Vedenov et al. 1961; Drummond & Rosenbluth 1962) is used to determine how the particle distribution changes due to the interaction with the Alfvén waves. Here the variables of the Vlasov equation are split into slowly varying average and first order fluctuation terms. Ref. Stix (1992) starts from the Vlasov equation, and provides a complete derivation of the full relativistic quasilinear kinetic equation describing the temporal evolution of the particle's distribution function due to interaction with the Alfvén waves at resonance. We added nonresonant terms following Yoon et al. (2009). The complete equation, that contains both the resonant (line 2) and the nonresonant (line 3) terms and is correct in both relativistic and non-relativistic regimes, is

$$\begin{aligned} \frac{\partial F}{\partial t} = & \frac{e^2}{4} \sum_l \int d\mathbf{k} \frac{1}{p_{\perp}} \left[\left(1 - \frac{k_{\parallel} p_{\parallel}}{\gamma m \omega} \right) \frac{\partial}{\partial p_{\perp}} + \frac{k_{\parallel} p_{\perp}}{\gamma m \omega} \frac{\partial}{\partial p_{\parallel}} \right] \\ & \times \left\{ p_{\perp} \left[\pi \delta \left(\omega - l \omega_c - \frac{k_{\parallel} p_{\parallel}}{\gamma m} \right) |E_k|^2 \right. \right. \\ & \left. \left. - \frac{\partial}{\partial \omega} \left(PV \left(\frac{1}{\omega - l \omega_c - \frac{k_{\parallel} p_{\parallel}}{\gamma m}} \right) \right) \frac{\partial |E_k|^2}{\partial t} \right] \right. \\ & \left. \times \left[\left(1 - \frac{k_{\parallel} p_{\parallel}}{\gamma m \omega} \right) \frac{\partial}{\partial p_{\perp}} + \frac{k_{\parallel} p_{\perp}}{\gamma m \omega} \frac{\partial}{\partial p_{\parallel}} \right] F \right\}. \quad (1) \end{aligned}$$

Here $\omega_c = eB_0/\gamma mc$ is the particle gyration frequency; ω is the Alfvén wave frequency (whose dispersion relation is described in Section 2.1 below); PV denotes a Principal Value; k_{\parallel} is the wavenumber in the direction parallel to the background magnetic field, and $l = 1, 2, \dots$ is the harmonic number. The integration is over the Alfvénic wavevector \mathbf{k} , which is assumed to be in the direction parallel to \mathbf{B}_0 , as described above.

The equation is governed by whether the resonance condition $\omega - l \omega_c - \frac{k_{\parallel} p_{\parallel}}{\gamma m} = 0$ is satisfied. While this is the case in many plasmas, it is not in FRB emission regions. Due to strong magnetic fields, plasmas in these environments have a low β . For Alfvén waves in such a plasma, the inequalities $\omega_c \gg \omega$ and $\omega_c \gg \frac{k_{\parallel} p_{\parallel}}{\gamma m}$ hold (Wu & Yoon 2007), resulting in no contribution from the resonant term. The presence of the $\frac{\partial |E_k|^2}{\partial t}$ term requires that the Alfvén wave electric field varies temporally in the nonresonant case, a restriction that is not found in the resonant regime.

To ensure that the above conditions are always satisfied, the maximum wavenumber of the Alfvén wave, k_{\max} must not be too large. Assuming an Alfvén relation of $w = kc$ in the highly magnetized and relativistic case, the condition for the nonresonant interaction to remain dominant becomes $\omega_c \gg k_{\max} c$. We can further assume that the Alfvén wave is generated by some instability of the neutron star such as a quake (Blaes et al. 1989). Thus the wavelength $\lambda = \xi R_*$ will be some fraction ξ of the neutron star radius R_* , with a corresponding wavenumber of $k \sim 2\pi/(\xi R_*)$. The condition of validity thus becomes $2\pi c/(\omega_c R_*) \ll \xi$. Using fiducial values

of $R_* = 10^6$ cm and $\omega_c = 10^9$ rad s⁻¹, which is appropriate for FRBs, we obtain the condition $\xi \gg 2 \times 10^{-4} \omega_{c,9}^{-1} R_{*,6}^{-1}$, where we use the convention $Q = 10^x Q_x$ in cgs units. Typical wavelengths of waves in neutron star crusts are estimated to be of the order of $\lambda \sim 10^4$ cm to $\lambda \sim 10^7$ cm, the equivalent of $\xi \sim 10^{-2} R_{*,6}^{-1}$ to $\xi \sim 10 R_{*,6}^{-1}$ (Blaes et al. 1989; Beloborodov 2023b). Therefore, the maximum value of k_{\max} will not exceed a fraction of ω_c/c , confirming that the interaction will remain in the nonresonant regime. In low magnetization cases, the value of k_{\max} will be lower due to the reduced Alfvén velocity, resulting in an even less restrictive limit.

The nonresonant term can itself be simplified through the approximation (Yoon et al. 2009):

$$\frac{\partial}{2\partial\omega} \left(PV \left(\frac{1}{\omega - l\omega_c - \frac{k_{\parallel} p_{\parallel}}{\gamma m}} \right) \right) \frac{\partial |E_k|^2}{\partial t} \approx -\frac{1}{2\omega_c^2} \frac{\partial |E_k|^2}{\partial t}, \quad (2)$$

where the higher harmonics' ($l = 2, 3, \dots$) contribution is neglected.

In order to present equation (1) more clearly, we expand the equation and separate the terms, using only the dominant ($l = 1$) harmonic. The resulting expression is

$$\begin{aligned} \frac{\partial F}{\partial t} = & \frac{1.16 \times 10^6}{\omega_{c,9}^2} \int d\mathbf{k} \left\{ \left(\frac{I_1 \left(2 + \frac{q_{\perp}^2}{\gamma^2} \right)}{\gamma} - 2 \frac{I_2 q_{\parallel}}{\gamma^2} \right) \frac{\partial F}{\partial q_{\parallel}} \right. \\ & + \left[\frac{1}{q_{\perp}} \left(I_3 \left(1 + 2 \frac{q_{\perp}^2}{\gamma^2} \right) + \frac{I_2 q_{\parallel}^2}{\gamma^2} - \frac{I_1 q_{\parallel} \left(2 + \frac{q_{\perp}^2}{\gamma^2} \right)}{\gamma} \right) \right. \\ & - \left. \frac{I_2 q_{\perp}}{\gamma^2} \right] \frac{\partial F}{\partial q_{\perp}} \\ & + \frac{I_2 q_{\perp}^2}{\gamma^2} \frac{\partial^2 F}{\partial q_{\perp}^2} \\ & + \left(I_3 + \frac{I_2 q_{\parallel}^2}{\gamma^2} - 2 \frac{I_1 q_{\parallel}}{\gamma} \right) \frac{\partial^2 F}{\partial q_{\parallel}^2} \\ & \left. + \left(2 \frac{I_1 q_{\perp}}{\gamma} - 2 \frac{I_2 q_{\perp} q_{\parallel}}{\gamma^2} \right) \frac{\partial^2 F}{\partial q_{\parallel} \partial q_{\perp}} \right\}, \quad (3) \end{aligned}$$

where the factor $\frac{1.16 \times 10^6}{\omega_{c,9}^2} = \frac{e^2}{8\pi c m^2 \omega_c^2}$, $q = p/mc = \gamma \frac{v}{c} = \gamma\beta$, and $I_1 = \int d\mathbf{k} \frac{\partial |E_k|^2}{\partial t} \frac{k_{\parallel}}{\omega}$, $I_2 = \int d\mathbf{k} \frac{\partial |E_k|^2}{\partial t} \frac{ck_{\parallel}^2}{\omega^2}$ and $I_3 = \int d\mathbf{k} \frac{\partial |E_k|^2}{\partial t} \frac{1}{c}$. equation (3) is correct in the limit of strong magnetic field, in both the relativistic and non-relativistic regimes.¹

Each line in equation (3) describes a different component of the overall evolution, which we respectively denote as $\left(\frac{\partial F}{\partial t}\right)_x$. From top to bottom, these terms describe parallel advection $\left(\frac{\partial F}{\partial t}\right)_{\parallel,1}$, perpendicular advection $\left(\frac{\partial F}{\partial t}\right)_{\perp,1}$, parallel diffusion $\left(\frac{\partial F}{\partial t}\right)_{\parallel,2}$, perpendicular diffusion $\left(\frac{\partial F}{\partial t}\right)_{\perp,2}$ and a mixed term $\left(\frac{\partial F}{\partial t}\right)_{mix}$.

¹ There is a typographical error in equation (3) of Long & Pe'er (2023), causing the discrepancy with equation (3) of this work which has extra terms on lines 1 and 2. The equation presented above is the correct version.

2.1 Dispersion relation of the Alfvén waves

In order to solve the time evolution of the distribution function described by equation (3), one needs to evaluate the integrals I_1 , I_2 and I_3 . The integrals I_1 and I_2 are calculated using either the non-relativistic Alfvén dispersion relation $\omega = kv_A$, where v_A is the Alfvén velocity, or the full relativistic solution given by (Asenjo et al. 2009; Muñoz et al. 2014),

$$\omega^2 - c^2 k^2 = \sum_s \omega_{p(s)}^2 \frac{\omega'}{f_s \bar{\gamma}_s \omega' - \Omega_s}. \quad (4)$$

Here, the subscript s denotes the particle species; $\omega' = \omega - kv_0$; v_0 is the particles' bulk velocity (in case it is non-zero); $\omega_{p(s)} = \sqrt{4\pi n_s e^2 / m_s}$ is the plasma frequency; $f_s = K_3 \left(\frac{m_s c^2}{k_B T_s} \right) / K_2 \left(\frac{m_s c^2}{k_B T_s} \right)$ is the plasma's enthalpy; $\bar{\gamma}_s$ is the species Lorentz factor and $\Omega_s = q_s B_0 / m_s c$ is the species gyration frequency where q_s is the species charge. K_l denotes a modified Bessel function of the second kind of order l .

In the non-relativistic regime the ratio between the integrals is simply given by $I_1 = \frac{v_A}{c} I_2 = \frac{c}{v_A} I_3$. In this limit therefore $I_2 > I_1 > I_3$ for all $v_A < c$. This relationship also holds for the relativistic case provided that k_{\max} is sufficiently small that the $\omega - k$ relationship remains linear, which is the case for the parameter space examined in this work.

To demonstrate this, expanding equation (4) for a two species plasma gives

$$\omega^2 - c^2 k^2 = \omega_{p-}^2 \frac{\omega'}{f_- \bar{\gamma}_- \omega' - \Omega_-} + \omega_{p+}^2 \frac{\omega'}{f_+ \bar{\gamma}_+ \omega' - \Omega_+}, \quad (5)$$

where the subscript $+$ denotes the positively charged species and the subscript $-$ denotes the electrons. Defining $\mu = m_+/m_-$ as the mass ratio of the two species and assuming both species have equal f and $\bar{\gamma}$, the above equation can be written as

$$\omega^2 - \omega \left(\frac{\omega_{p+}^2}{f \bar{\gamma} \omega - \Omega_+} + \frac{\mu \omega_{p+}^2}{f \bar{\gamma} \omega + \mu \Omega_+} \right) - c^2 k^2 = 0, \quad (6)$$

for particles with zero bulk velocity. In the low frequency limit, $f \bar{\gamma} \omega < \Omega_+$, one can make the following approximations:

$$\begin{aligned} \frac{\omega_{p+}^2}{f \bar{\gamma} \omega - \Omega_+} & \approx -\frac{\omega_{p+}^2}{\Omega_+} \left(1 + \frac{f \bar{\gamma} \omega}{\Omega_+} \right) \\ \frac{\mu \omega_{p+}^2}{f \bar{\gamma} \omega + \mu \Omega_+} & \approx \frac{\omega_{p+}^2}{\Omega_+} \left(1 - \frac{f \bar{\gamma} \omega}{\mu \Omega_+} \right). \end{aligned} \quad (7)$$

The term in brackets in equation (6) can therefore be written as

$$\left(\frac{\omega_{p+}^2}{f \bar{\gamma} \omega - \Omega_+} + \frac{\mu \omega_{p+}^2}{f \bar{\gamma} \omega + \mu \Omega_+} \right) \approx -\frac{f \bar{\gamma} \omega \omega_{p+}^2}{\Omega_+^2} \left(1 + \frac{1}{\mu} \right), \quad (8)$$

and the entire dispersion relation can therefore be approximated as

$$\omega^2 \left(1 + \frac{f \bar{\gamma} \omega_{p+}^2}{\Omega_+^2} \left(1 + \frac{1}{\mu} \right) \right) \approx c^2 k^2, \quad (9)$$

showing that the relativistic Alfvén wave dispersion relation is linear in the low frequency regime of interest to this work, with a corresponding relativistic Alfvén velocity of $v_{A,rel} = c \left(1 + \frac{f \bar{\gamma} \omega_{p+}^2}{\Omega_+^2} \left(1 + \frac{1}{\mu} \right) \right)^{-1/2}$.

2.2 Spectrum of the Alfvén wave

For the results presented in this work we model the Alfvén waves as having a flat spectrum between the minimum and maximum wavenumbers, k_{\min} and k_{\max} . This is chosen both as a plausible test scenario as the true spectrum is unknown and for ease of comparing results. Crucially, the outcome of the wave-particle interaction is insensitive to the precise spectrum chosen provided that the Alfvén wave dispersion relation is linear, as in this case $I_1 = \frac{v_{A,rel}}{c} I_2 = \frac{c}{v_{A,rel}} I_3$ always holds. As a concrete demonstration, consider waves having a power law spectrum where the spectral electric field is given by $E_k = E_0 k^{-\varphi}$, with E_0 constant. Using $\frac{\partial |E_k|^2}{\partial t} = 2\Gamma_k E_k^2$, where Γ_k is the spectral growth rate of the Alfvén wave, the terms I_1 , I_2 and I_3 become

$$\begin{aligned} I_1 &= 2 \int dk \Gamma_k E_0^2 k_{\parallel}^{-2\varphi} \frac{k_{\parallel}}{\omega} = \frac{2}{v_{A,rel}} \int dk \Gamma_k E_0^2 k_{\parallel}^{-2\varphi}, \\ I_2 &= 2 \int dk \Gamma_k E_0^2 k_{\parallel}^{-2\varphi} \frac{c k_{\parallel}^2}{\omega^2} = \frac{2c}{v_{A,rel}^2} \int dk \Gamma_k E_0^2 k_{\parallel}^{-2\varphi}, \\ I_3 &= 2 \int dk \Gamma_k E_0^2 \frac{k_{\parallel}^{-2\varphi}}{c} = \frac{2}{c} \int dk \Gamma_k E_0^2 k_{\parallel}^{-2\varphi}, \end{aligned} \quad (10)$$

with ratios identical to the flat spectrum case. Note that we explicitly used the assumption that the Alfvén waves propagation direction is parallel to the background magnetic field.

The magnitude of each I_x term ($x = 1, 2, 3$), and thus the time-scale of the process, is also independent of the precise spectrum provided that: (i) the spectral growth rate Γ_k is a constant and (ii) the total energy contained in the spectra in question is the same. For spectra not satisfying these requirements, the appropriate time-scales can be retrieved from the flat spectrum results presented in section 4.2 simply by multiplying by a factor of

$$\frac{\int_{k_{\min,0}}^{k_{\max,0}} dk \Gamma_{k,0} |E_0|^2}{\int_{k_{\min,1}}^{k_{\max,1}} dk \Gamma_{k,1} |E_k|^2}, \quad (11)$$

where the subscript 0 refers to the flat spectrum and the subscript 1 refers to the other spectrum of interest.

To illustrate a case which does satisfy the above requirements, we continue the example of a power law spectrum presented in equation (10) with the added constraint that Γ_k is constant. The I_x terms can be written as

$$\begin{aligned} I_1 &= \frac{2\Gamma_k E_0^2}{(-2\varphi + 1)v_{A,rel}} (k_{\max}^{-2\varphi+1} - k_{\min}^{-2\varphi+1}), \\ I_2 &= \frac{2\Gamma_k c E_0^2}{(-2\varphi + 1)v_{A,rel}^2} (k_{\max}^{-2\varphi+1} - k_{\min}^{-2\varphi+1}), \\ I_3 &= \frac{2\Gamma_k E_0^2}{(-2\varphi + 1)c} (k_{\max}^{-2\varphi+1} - k_{\min}^{-2\varphi+1}), \end{aligned} \quad (12)$$

and the ratio $I_{x,flat}/I_{x,power\ law}$ given by

$$\frac{I_{x,flat}}{I_{x,power\ law}} = \frac{(k_{\max}^{-2\varphi+1} - k_{\min}^{-2\varphi+1})}{(k_{\max} - k_{\min})(1 - 2\varphi)}. \quad (13)$$

This is the same factor obtained when comparing the energy density of a flat spectrum $E_k = E_0$ and power law spectrum

$$E_k = E_0' k^{-\varphi}:$$

$$\begin{aligned} \int dk E_0'^2 &= \int dk E_0'^2 k^{-2\varphi}, \\ E_0'^2 (k_{\max} - k_{\min}) &= E_0'^2 \frac{(k_{\max}^{-2\varphi+1} - k_{\min}^{-2\varphi+1})}{(1 - 2\varphi)}, \\ \frac{E_0'^2}{E_0'^2} &= \frac{(k_{\max}^{-2\varphi+1} - k_{\min}^{-2\varphi+1})}{(k_{\max} - k_{\min})(1 - 2\varphi)}, \end{aligned} \quad (14)$$

where we have assumed an equal wavenumber range in both cases. This demonstrates that the magnitudes of the I_x terms, and thus the time-scale of the interaction, are independent of the Alfvén wave spectrum in this case.

3 METHODS AND ANALYSIS

3.1 Solving the nonresonant wave-particle interaction

To solve equation (3), a number of numerical schemes were used. These include the Crank-Nicolson, upwind differencing and fully implicit finite difference methods (Press et al. 2007). The equation was solved with MATLAB on a term by term basis. The initial conditions are the initial distribution function F_0 , which is taken to be a Maxwell-Jüttner distribution with a normalized temperature $\theta = \frac{k_B T}{mc^2}$; the magnetization $\sigma = \Omega^2/\omega_p^2$; as well as k_{\max} and k_{\min} . We further assume a single temperature and density describing all species. The time units used are given in terms of $\Omega\tau$. Here $\tau = \bar{\Gamma}\eta t$, where $\bar{\Gamma} = \Gamma/\Omega \ll 1$ is the temporal growth rate of the Alfvén waves relative to the gyration frequency Ω and $\eta = |E_k|^2/B_0^2 \ll 1$ is the normalized wave energy. Improvements to the stability of the numerical scheme allowed higher resolutions and longer times to be achieved compared to the results presented in our previous proof of concept work (Long & Pe'er 2023).

The distribution function at some time τ is calculated by solving equation (3). This requires calculating the values for the integrals I_1 , I_2 and I_3 . We use the dispersion relation (equation (4)) as discussed in Section 2.1. While the values of these integrals determine the time scale for reaching a steady state, their ratio determines the amount of energy available in the population inversion.

The ratio I_2/I_1 is presented in Fig. 1, showing its dependence on both magnetization and temperature. This ratio is equal to $I_2/I_1 = c/v_{A,rel}$ in the linear regime, although the numerical results we show are general. The value of I_2/I_1 decreases as the magnetization increases, asymptoting to a value of $I_2/I_1 = 1$ at a temperature dependent magnetization of $\sigma \gtrsim 10$. Physically, this occurs when $v_{A,rel}$ approaches c . For lower magnetizations $\sigma \lesssim 1$, the relationship becomes $I_2/I_1 \propto \sigma^{-1/2}$. This is to be expected as $v_{A,rel} \propto \sigma^{1/2}$. In this regime, the value of I_2/I_1 increases with temperature for all magnetizations in this range due to the decrease in $v_{A,rel}$ at higher temperatures.

After solving equation (3) numerically using the above methods, we calculate the fraction of energy contained in the crescent shaped population inversion, f_{inv} , as well as the time taken to reach this value. To obtain f_{inv} we take the distribution obtained through solving equation (3) and calculate its total kinetic energy, $E_{tot} = \int d\mathbf{p}(\gamma(\mathbf{p}) - 1)F(\mathbf{p})$. We compare this value to the total kinetic energy of another distribution with the same widths as the actual distribution

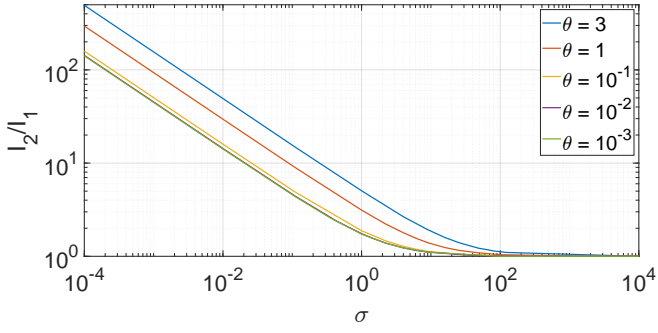


Figure 1. The value of I_2/I_1 versus magnetization σ for a wavenumber range $0 < k < 0.01\Omega/c$, showing how for a given σ , I_2/I_1 increases with temperature. For $\sigma \lesssim 1$, the relationship between the two quantities is $I_2/I_1 \propto \sigma^{-1/2}$.

in both the parallel and perpendicular directions. However, this comparison distribution is centred at the coordinates of the maximum value of the actual distribution for all values of q_\perp . The resulting distribution is therefore similar to a Bi-Maxwellian distribution with non-constant widths as the contributions from the crescent shaped arms, which are centred at increasingly large values of $q_\parallel > 0$ as $|q_\perp|$ increases, have been removed. We denote the total kinetic energy of this modified distribution as E_{bi} . f_{inv} is then retrieved by comparing the two energy values through $f_{inv} = (E_{tot} - E_{bi})/E_{tot}$. This quantity is therefore the amount of excess energy contained in the crescent part of the deformed distribution only, and does not include any contributions from changes in energy that are not associated with the population inversion.

Results were obtained across a large parameter space, examining temperatures ranging from $\theta = 10^{-2}$ to $\theta = 3$ and magnetizations greater than $\sigma \approx 10^{-4}$. As a demonstration of the evolution of the initial Maxwell-Jüttner distribution, Fig. 2 shows contour plots of the distribution at $\tau = 0$, $\tau = \tau_{max}/10$ and $\tau = \tau_{max}$, where τ_{max} is the time taken to reach the asymptotic value of f_{inv} . The results in Fig. 2 are for an initial temperature of $\theta = 10^{-1}$ and $I_2/I_1 = 1$, equivalent to $\sigma \gtrsim 10^2$. The formation of the crescent shape is visible through the extension of the initial distribution to larger values of $|q_\perp|$ for $q_\parallel > 0$, with the arms of the crescent expanding as the distribution continues to evolve.

3.2 Detailed analysis of the nonresonant interaction at high magnetizations

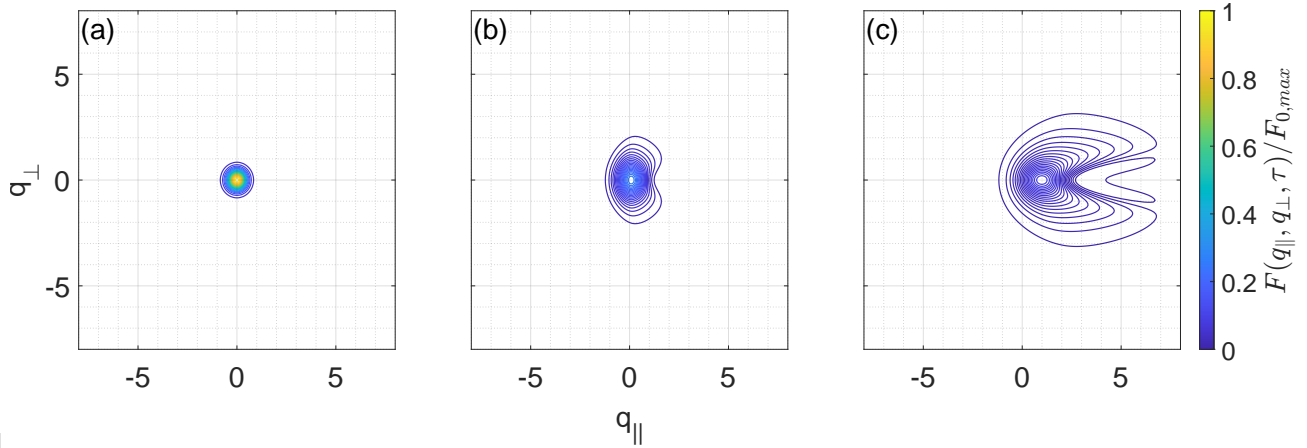
We first examine the overall evolution of the particle distribution function. A plot of $\frac{\partial F_0}{\partial t}$ is shown in Fig. 3 for an initial Maxwell-Jüttner distribution with temperature $\theta = 0.1$ and $I_2/I_1 = 1$, the same parameters as displayed in Fig. 2. These results are thus applicable for high magnetizations of $\sigma > 10^2$. As shown in Fig. 3, the primary outcome of the wave particle interaction is to transfer particles from regions of low perpendicular momentum, $|q_\perp| \lesssim 0.5$, and negative parallel momentum, $q_\parallel < 0$ (the blue region in Fig. 3), to higher perpendicular momenta (in both the positive and negative directions) through pitch angle diffusion. The resulting regions of positive $\frac{\partial F_0}{\partial t}$ are primarily in the $q_\parallel > 0$ half of the momentum space. The interaction also results in a bulk momentum in the parallel direction, as can be seen in Fig. 2c where the peak of the distribution is located at $q_\parallel \sim 1$.

To determine how the nonresonant interaction results in the overall evolution shown in Fig. 3, it is necessary to compare the terms in equation (3) to each other. Examining the contributions to $\frac{\partial F_0}{\partial t}$ from each individual term in Fig. 4 allows us to determine which terms are most crucial to the formation of the population inversion. In our previous work (Long & Pe'er 2023), we focused on the behaviour of the $(\frac{\partial F_0}{\partial t})_{\parallel,1}$ term, as it is the largest in magnitude for all values of $I_2/I_1 \gtrsim 1$. Here, we undertake a more detailed analysis of the relative importance of each term. All five terms are presented in Fig. 4a to 4e, showing $(\frac{\partial F_0}{\partial t})_{\parallel,1}$, $(\frac{\partial F_0}{\partial t})_{\perp,1}$, $(\frac{\partial F_0}{\partial t})_{\parallel,2}$, $(\frac{\partial F_0}{\partial t})_{\perp,2}$ and $(\frac{\partial F_0}{\partial t})_{mix}$ respectively for the same set of parameters as presented in Fig. 3. We note that $\frac{\partial F_0}{\partial t}$ is symmetric in the perpendicular direction, but asymmetric in the parallel direction, which is important to the formation of the crescent shape seen in Fig. 2. Indeed, several of the terms in equation (3) are asymmetric about $q_\parallel = 0$. Both perpendicular terms have a maximum magnitude offset from $q_\parallel = 0$, as can be seen in Fig. 4b and 4d. This offset is due to the I_3 terms in both coefficients, shown on lines 2 and 4 of equation (3).

However, the only two terms where the maximum value of $\frac{\partial F_0}{\partial t}$ is centred at $|q_\perp| > 0$ and $q_\parallel > 0$ are the parallel diffusion term $(\frac{\partial F_0}{\partial t})_{\parallel,2}$, displayed in Fig. 4c, and the mixed term $(\frac{\partial F_0}{\partial t})_{mix}$, shown in Fig. 4e. The parallel diffusion term is considerably lower in magnitude than the mixed term, and furthermore is symmetric in both directions. As none of the other terms provide the necessary positive regions of $\frac{\partial F_0}{\partial t}$ at $|q_\perp| > 0$ and $q_\parallel > 0$, this leads us to conclude that $(\frac{\partial F_0}{\partial t})_{mix}$ is the crucial term that determines the level of population inversion that is formed. This is the case even though it is not the largest term for any set of parameters. The overall form of $\frac{\partial F_0}{\partial t}$ in Fig. 3 is dominated by the perpendicular terms, but the contribution of the mixed term provides the element that results in the maximum value of $\frac{\partial F_0}{\partial t}$ being centred at a value of $q_\parallel > 0$ rather than $q_\parallel = 0$. At this high magnetization, the impact of the substantial region of positive $\frac{\partial F_0}{\partial t}$ from the parallel advection term in Fig. 4a is cancelled out by the equivalent negative $\frac{\partial F_0}{\partial t}$ in the same region from both perpendicular terms and the mixed term.

3.3 Examining the magnetization and temperature dependence

To obtain an efficient population inversion with a high value of f_{inv} , one requires an evolution of the particle distribution in both the parallel and perpendicular directions. The form of $\frac{\partial F_0}{\partial t}$ (i.e., the general regions in momentum space where the change in the distribution function is positive or negative) is strongly dependent on the magnetization. This can be seen in the progression of Fig. 3, 5a, 5b, 5c and 5d which show $\frac{\partial F_0}{\partial t}$ for $I_2/I_1 = 1$, $I_2/I_1 = 2$, $I_2/I_1 = 3$, $I_2/I_1 = 10$ and $I_2/I_1 = 30$ respectively. The temperature in each case is $\theta = 10^{-1}$. The black crosses in each figure show the coordinates of the maximum value $(\frac{\partial F_0}{\partial t})_{max}$. As the magnetization decreases and I_2/I_1 increases, the main positive regions of $\frac{\partial F_0}{\partial t}$ move from being predominantly in the perpendicular directions to the positive parallel direction. This evolution can be quantified by the coordinates of $(\frac{\partial F_0}{\partial t})_{max}$, denoted as $q_{\parallel,max}$ and $q_{\perp,max}$. The angle this point makes with the



[b]
Figure 2. Contour plots of the distribution function F for an initial Maxwell-Jüttner distribution in the high magnetization regime with $\theta = 10^{-1}$ and $I_2/I_1 = 1$. **Panel (a)** shows the initial distribution function F_0 ; **panel (b)** shows F at $\Omega\tau_{\max}/10$ and **panel (c)** shows the distribution at $\Omega\tau_{\max}$. $\Omega\tau_{\max}$ is the time taken to reach the asymptotic value of f_{inv} . The progression from the initial to the final timestep show the development of the arms of the crescent shaped population inversion. The values are normalized to the maximum initial value of $F_0(\theta = 0.1)$

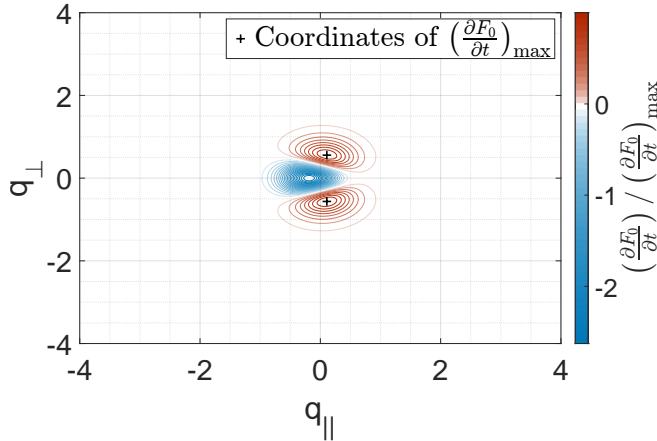


Figure 3. Contour plot of $\frac{\partial F_0}{\partial t}$ for a Maxwell-Jüttner distribution in the high magnetization regime for $\theta = 0.1$ and $I_2/I_1 = 1$. The values are normalized to the maximum value of $\frac{\partial F_0}{\partial t}$. The coordinates of the maximum value of $\frac{\partial F_0}{\partial t}$ are marked by the black crosses (as $\frac{\partial F_0}{\partial t}$ is symmetric in the perpendicular direction there are 2 maxima). The positive contribution of this term is strongest off-axis in the $q_{\parallel} > 0$ region, and will lead to an evolved distribution as in Fig. 2b.

q_{\parallel} axis is defined as $\alpha = \tan^{-1}\left(\frac{q_{\perp, \max}}{q_{\parallel, \max}}\right)$. This angle is presented in Fig. 6 as a function of the magnetization for a range of temperatures.

The angle α provides a description of the general form of $\frac{\partial F_0}{\partial t}$. The maximal value of the population inversion occurs for intermediate values of $0 < \alpha < \pi/2$ where a clear crescent shape can form. However, some inversion will occur even for extreme values of $\alpha = 0, \pi/2$, due to the contribution from the mixed term. As discussed in section 3.2, this provides the crucial positive regions of $\frac{\partial F}{\partial t}$ for $|q_{\perp}| > 0$ and $q_{\parallel} > 0$. The importance of $\left(\frac{\partial F_0}{\partial t}\right)_{mix}$ for different parameters is further discussed in section 3.4 below.

Fig. 6 shows the evolution of α for different particle temperatures. While the general form of $\frac{\partial F_0}{\partial t}$ is qualitatively the

same for different temperatures, the precise location of the positive and negative regions is temperature dependent. As can be seen, α increases towards $\frac{\pi}{2}$ as the temperature decreases, implying that the distribution function changes predominantly in the perpendicular direction, as described in previous works (e.g. Wu & Yoon 2007; Yoon et al. 2009). While for all parameters there are effects in both the parallel and perpendicular directions, the acceleration of particles in the perpendicular direction through pitch angle diffusion becomes stronger relative to the parallel processes at lower temperatures. This will affect both the angle α , as well as the widths of the particle distribution in the parallel and perpendicular directions, θ_{\parallel} and θ_{\perp} ². The results for the temperature dependence of α obtained match expectations from previous analyses in the non-relativistic regime which show that the temperature anisotropy $A = \theta_{\perp}/\theta_{\parallel}$ caused by the nonresonant interaction decreases as the temperature increases (Wang et al. 2006).

For all temperatures θ examined, α always decreases toward 0 as the magnetization decreases. This decrease is largely due to the behaviour of the parallel advection term $\left(\frac{\partial F_0}{\partial t}\right)_{\parallel,1}$. First, as I_2/I_1 increases, this term becomes positive for $q_{\parallel} > 0$, which is in contrast to the case for high magnetizations ($I_2/I_1 \sim 1$) where $\left(\frac{\partial F_0}{\partial t}\right)_{\parallel,1}$ is negative for $q_{\parallel} > 0$. This can be seen by examining the coefficient for this term on line 1 of equation (3). As I_2/I_1 increases, the term $2\frac{I_2 q_{\parallel}}{\gamma^2}$ becomes greater in magnitude than the other terms contributing to $\left(\frac{\partial F_0}{\partial t}\right)_{\parallel,1}$. As there is an additional factor of $-q_{\parallel}$ from the partial derivative $\frac{\partial F}{\partial q_{\parallel}}$ in the case of a Maxwell-Jüttner distribution, the dominance of this term results in $\left(\frac{\partial F_0}{\partial t}\right)_{\parallel,1}$ being positive across all of momentum space. This is shown in Fig. 7, which displays $\left(\frac{\partial F_0}{\partial t}\right)_{\parallel,1}$ for $I_2/I_1 = 30$. This figure also shows that $\left(\frac{\partial F_0}{\partial t}\right)_{\parallel,1}$ is centred at $q_{\perp} = 0$, contributing to a decrease in α . This is in contrast to the contribution from

² Note that at $t = 0$, $\theta_{\parallel} = \theta_{\perp} = \theta$, but they can differ with time.

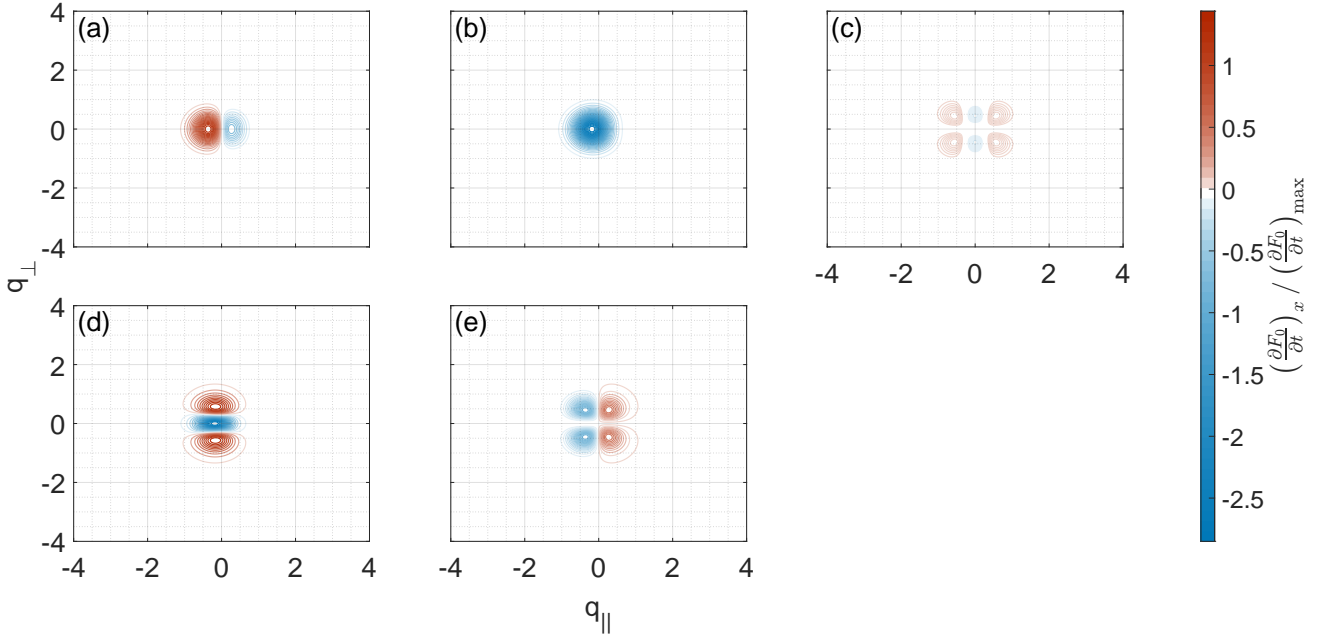


Figure 4. Contour plots of each individual term $\left(\frac{\partial F_0}{\partial t}\right)_x$ from equation (3). Each $\left(\frac{\partial F_0}{\partial t}\right)_x$ is calculated for a Maxwell-Jüttner distribution in the high magnetization regime with $\theta = 0.1$ and $I_2/I_1 = 1$. The values are normalized to the maximum value of the overall $\frac{\partial F_0}{\partial t}$. **Panel (a)** shows the parallel advection term $\left(\frac{\partial F_0}{\partial t}\right)_{\parallel,1}$. The contribution from this term consists of a strong $\frac{\partial F}{\partial t} > 0$ for $q_{\parallel} < 0$ and a weaker $\frac{\partial F}{\partial t} < 0$ for $q_{\parallel} > 0$. **Panel (b)** shows the perpendicular advection term $\left(\frac{\partial F_0}{\partial t}\right)_{\perp,1}$. This term has an entirely negative contribution to the change in the distribution for these parameters and thus does not contribute to the formation of the crescent shaped inversion. **Panel (c)** shows the parallel diffusion term $\left(\frac{\partial F_0}{\partial t}\right)_{\parallel,2}$. The maximum positive contribution for this term is strongest for $|q_{\perp}| > 0$, as in the overall $\frac{\partial F_0}{\partial t}$. However, this term is symmetric in both directions and is also relatively weak compared to the other terms in equation (3). **Panel (d)** shows the perpendicular diffusion term $\left(\frac{\partial F_0}{\partial t}\right)_{\perp,2}$. This term acts to symmetrically diffuse the particles in the perpendicular direction. Note the similarity to $\frac{\partial F_0}{\partial t}$ in Fig. 3, except for the location of the main regions where $\frac{\partial F_0}{\partial t} > 0$. Finally, **Panel (e)** shows the mixed term $\left(\frac{\partial F_0}{\partial t}\right)_{mix}$. The maximum positive contribution for this term is strongest for $|q_{\perp}| > 0$ and $q_{\parallel} > 0$, as in the overall $\frac{\partial F_0}{\partial t}$. This term is also considerably stronger than $\left(\frac{\partial F_0}{\partial t}\right)_{\parallel,2}$, which has a similar form in the $q_{\parallel} > 0$ part of the momentum space.

the parallel and mixed diffusion terms, which are not centred at $q_{\perp} = 0$ (see Fig. 4c and 4e respectively).

Furthermore, the parallel advection term increases in magnitude as I_2/I_1 increases, becoming larger than all others at $I_2/I_1 \sim 1.2$ for $\theta = 10^{-1}$. This can be seen in Fig. 8 where the maximum value of each term $\left(\frac{\partial F_0}{\partial t}\right)_{x,max}$ from equation (3) is plotted, with $\left(\frac{\partial F_0}{\partial t}\right)_{\parallel,1,max}$ shown by the solid blue line. These values in Fig. 8 are normalized to the overall $\left(\frac{\partial F_0}{\partial t}\right)_{max}$. The value of I_2/I_1 at which the parallel advection term becomes largest is temperature dependent, with the value increasing as the temperature decreases. The other major terms at $I_2/I_1 \sim 1$ are $\left(\frac{\partial F_0}{\partial t}\right)_{\perp,2}$ and $\left(\frac{\partial F_0}{\partial t}\right)_{mix}$, shown by the solid purple and green lines in Fig. 8 respectively. As both these terms are second order, they are relatively stronger at lower temperatures due to the factor of θ^{-2} from the derivatives $\frac{\partial^2 F}{\partial q_{\parallel}^2}$ and $\frac{\partial^2 F}{\partial q_{\perp}^2}$. This implies that the ratio I_2/I_1 above which the parallel advection term becomes dominant increases at lower temperatures. The increase in strength of the parallel advection term, as well as the relative weakness of the mixed term as the magnetization decreases results in $\left(\frac{\partial F_0}{\partial t}\right)_{max}$ shifting closer to $|q_{\perp}| = 0$. As is shown in Fig. 5c and 5d, this combi-

nation of factors results in an overall initial evolution that is closer to parallel advection in the low magnetization parameter space, though pitch angle diffusion is still occurring on a smaller scale.

The reduction in the relative strength of the pitch angle diffusion relative to the parallel processes when $I_2/I_1 \gg 1$ results in evolved distributions that do not display the obvious crescent shapes observed at high magnetizations (such as in Fig. 2c), as discussed in our previous work (Long & Pe'er 2023). However, particles do still continue to be moved to higher perpendicular momenta for $q_{\parallel} > 0$ even when $\alpha = 0$. As a result, the population inversion still can form, though with much reduced values of f_{inv} , as is shown in our numerical results presented in Section 4.1.

To summarize the conclusions of the previous paragraphs, the acceleration of particles to larger perpendicular momenta values becomes relatively stronger both as the magnetization increases and the temperature decreases, resulting in an increase in α up to a maximum value of $\alpha = \pi/2$. This value however does not correspond to the most efficient population inversion as the resulting evolution is almost entirely perpendicular, while for the formation of the population inversion some contribution from the mixed and parallel terms is nat-

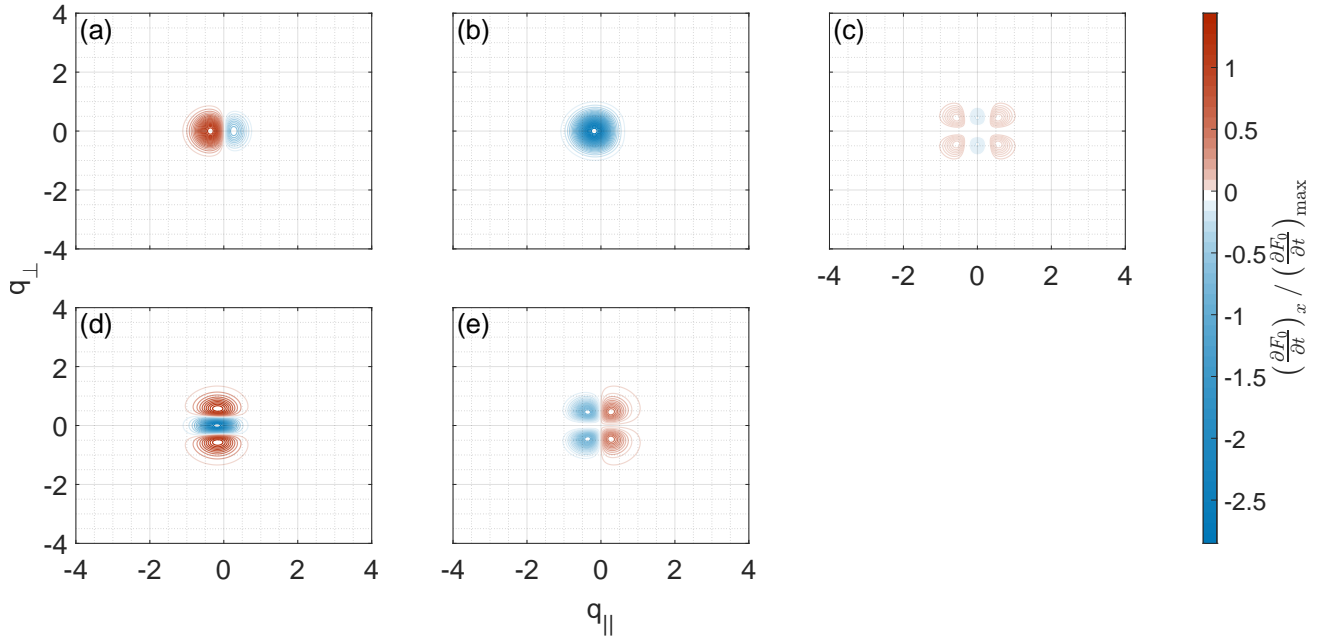


Figure 5. Contour plots of $\frac{\partial F_0}{\partial t}$ for Maxwell-Jüttner distributions with $\theta = 0.1$. **Panel (a)** shows $\frac{\partial F_0}{\partial t}$ for $I_2/I_1 = 2$, **panel (b)** shows $\frac{\partial F_0}{\partial t}$ for $I_2/I_1 = 3$, **panel (c)** shows $\frac{\partial F_0}{\partial t}$ for $I_2/I_1 = 10$ and **panel (d)** shows $\frac{\partial F_0}{\partial t}$ for $I_2/I_1 = 30$. In each case the values are normalized to the maximum value of $\frac{\partial F_0}{\partial t}$. The coordinates of the maximum value of $\frac{\partial F_0}{\partial t}$ are marked by the black crosses (as $\frac{\partial F_0}{\partial t}$ is symmetric in the perpendicular direction there are 2 maxima for $I_2/I_1 = 2$ and $I_2/I_1 = 3$). The decrease in α with increasing I_2/I_1 (equivalent to decreasing magnetization) is visible in the progression from panel (a) to panel (c) and (d), with $\alpha = 0$ for $I_2/I_1 = 10$ and $I_2/I_1 = 30$.

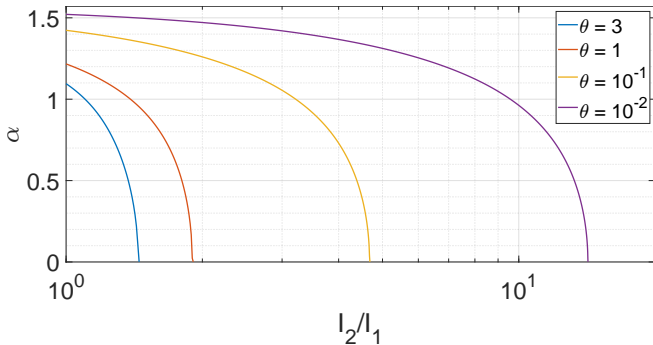


Figure 6. The angle $\alpha = \tan^{-1} \left(\frac{q_{\perp, \max}}{q_{\parallel, \max}} \right)$ is plotted versus I_2/I_1 for temperatures ranging from $\theta = 10^{-2}$ to $\theta = 3$. The solution becomes closer to perpendicular ($\alpha = \pi/2$) at lower temperatures as well as at higher magnetizations (lower values of I_2/I_1).

usually required to produce a crescent shape. The maximum value of f_{inv} is therefore obtained in the range $0 < \alpha < \pi/2$. We note that these results are the equivalent of the mechanism becoming less efficient as the plasma β increases, a result also seen in the non-relativistic regime (Wang & Wu 2009). We also emphasize that the maximum value of f_{inv} is not solely dependent on α , but also strongly depends on the mixed term as discussed in detail in Sections 3.2 and 3.4.

3.4 The mixed term and formation of a population inversion

Based on our previous analysis in section 3.2, the mixed term is a crucial element to the formation of the popula-

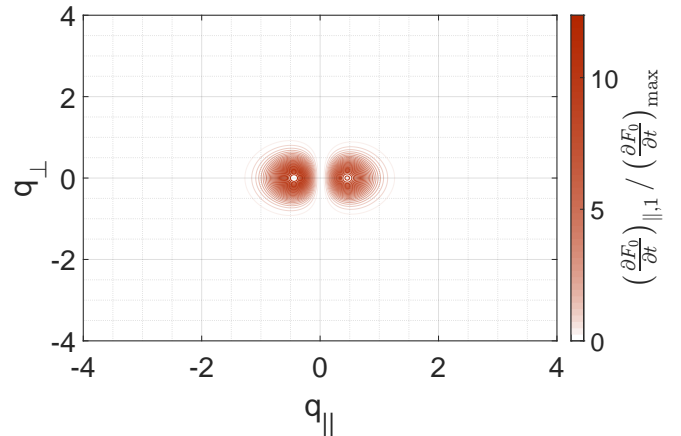


Figure 7. Contour plot of $\left(\frac{\partial F_0}{\partial t}\right)_{\parallel,1}$ for a Maxwell-Jüttner distribution in the low/intermediate magnetization regime for $\theta = 0.1$ and $I_2/I_1 = 30$. The values are normalized to the maximum value of $\frac{\partial F_0}{\partial t}$. In contrast to the case in Fig. 4a where $I_2/I_1 = 1$, for these parameters the contribution from this term consists of a strong $\left(\frac{\partial F_0}{\partial t}\right) > 0$ for both positive and negative q_{\parallel} .

tion inversion. We emphasize that the mixed term in general is not the largest in magnitude and as such does not dominate the overall form of the evolved distribution, especially at lower magnetizations. However, it provides the necessary positive $\frac{\partial F_0}{\partial t}$ for $|q_{\perp}| > 0$ and $q_{\parallel} > 0$ that leads to the crescent shape of the distribution. Furthermore, we show in Section 4 below that the trends followed by the mixed term closely match our numerical results. In order to examine the parametric dependence of this term, it is useful

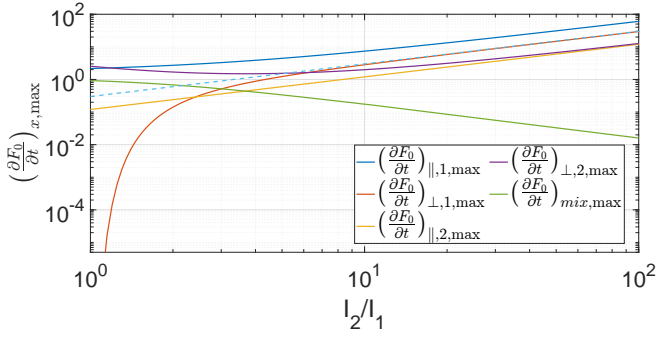


Figure 8. Plot of the the maximum value of every term in equation (3), normalized to the maximum value of the total $(\frac{\partial F_0}{\partial t})_{\text{max}}$. The dashed cyan line shows a fit of $(\frac{\partial F_0}{\partial t})_{\perp,1,\text{max}} \propto I_2/I_1$. This trend is followed by all terms except the mixed one for $I_2/I_1 \gg 1$. These values are calculated for a temperature of $\theta = 10^{-1}$. As the temperature increases, the first order terms $(\frac{\partial F_0}{\partial t})_{\parallel,1}$ and $(\frac{\partial F_0}{\partial t})_{\perp,1}$ will become stronger relative to the others, though the overall trends will be unchanged.

to compare its maximum value $(\frac{\partial F_0}{\partial t})_{\text{mix,max}}$ to that of the other terms. Fig. 9 presents the ratio of $(\frac{\partial F_0}{\partial t})_{\text{mix,max}}$ to the parallel and perpendicular terms $(\frac{\partial F_0}{\partial t})_{\parallel,\text{max}}$ and $(\frac{\partial F_0}{\partial t})_{\perp,\text{max}}$ as well to the overall $(\frac{\partial F_0}{\partial t})_{\text{max}}$ and the sum of all the other terms except the mixed term $(\frac{\partial F_0}{\partial t} - (\frac{\partial F_0}{\partial t})_{\text{mix}})_{\text{max}}$. Here $(\frac{\partial F_0}{\partial t})_{\parallel,\text{max}} = ((\frac{\partial F_0}{\partial t})_{\parallel,1} + (\frac{\partial F_0}{\partial t})_{\parallel,2})_{\text{max}}$ is the maximum value of the combined parallel terms and $(\frac{\partial F_0}{\partial t})_{\perp,\text{max}} = ((\frac{\partial F_0}{\partial t})_{\perp,1} + (\frac{\partial F_0}{\partial t})_{\perp,2})_{\text{max}}$ is the maximum value of combined perpendicular terms. We combine these terms for clarity of presentation as all the individual terms follow the same trends for $I_2/I_1 \gg 1$, as shown in Fig. 8.

In all cases except that of the comparison to the overall $(\frac{\partial F_0}{\partial t})_{\text{max}}$, the ratio is proportional to $(I_2/I_1)^{-2}$ at large values of I_2/I_1 ($I_2/I_1 \gtrsim 6$ for $\theta = 0.1$ as in Fig. 9). This is the equivalent of $(\frac{\partial F_0}{\partial t})_{\text{mix,max}} / (\frac{\partial F_0}{\partial t})_{\text{max}} \propto \sigma$ at these low and intermediate magnetizations, as $I_2/I_1 \propto \sigma^{-1/2}$ for $\sigma \ll 1$. As I_2/I_1 approaches 1, equivalent to higher magnetizations of $\sigma \gtrsim 1$, the ratio flattens out, becoming more weakly dependent on I_2/I_1 (see Fig. 1 for the temperature dependent I_2/I_1 - σ relationship). These results are derived semi-analytically in Appendix A below.

These trends are true for all temperatures, though the magnetization at which the linear relationship begins is temperature dependent. This can be seen in Fig. 10, which presents the ratio $(\frac{\partial F_0}{\partial t})_{\text{mix,max}} / (\frac{\partial F_0}{\partial t})_{\perp,\text{max}}$ for different temperatures. The choice of this specific ratio in Fig. 10 and in Section 4 below is because the other ratios $(\frac{\partial F_0}{\partial t})_{\text{mix,max}} / (\frac{\partial F_0}{\partial t})_{\parallel,\text{max}}$ and $(\frac{\partial F_0}{\partial t})_{\text{mix,max}} / (\frac{\partial F_0}{\partial t} - (\frac{\partial F_0}{\partial t})_{\text{mix}})_{\text{max}}$ show the same trends, and thus carry no new information. An increase in the value of I_2/I_1 at which the $(\frac{\partial F_0}{\partial t})_{\text{mix,max}} / (\frac{\partial F_0}{\partial t})_{\perp,\text{max}} \propto (I_2/I_1)^{-2}$ relationship begins can be seen as the temperature decreases.

To clarify this behaviour in terms of a more intuitive physical quantity, the same ratio is plotted in Fig. 11 versus the relativistic magnetization $\sigma_{\text{rel}} = \sigma/\gamma_{\text{av}}$, where γ_{av} is the average Lorentz factor of the initial distribution. This shows the

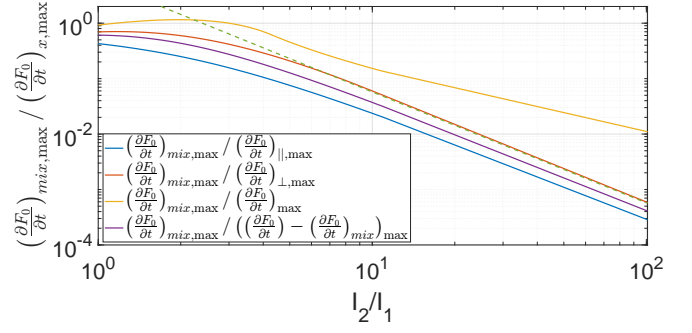


Figure 9. Plot of the ratio of $(\frac{\partial F_0}{\partial t})_{\text{mix,max}}$ for the mixed term to the maximum value of the parallel terms $(\frac{\partial F_0}{\partial t})_{\parallel,\text{max}}$ (blue), perpendicular terms $(\frac{\partial F_0}{\partial t})_{\perp,\text{max}}$ (orange), overall solution $(\frac{\partial F_0}{\partial t})_{\text{max}}$ (yellow) and $((\frac{\partial F_0}{\partial t}) - (\frac{\partial F_0}{\partial t})_{\text{mix}})_{\text{max}}$ (purple). The dashed green line indicates a fit of $(\frac{\partial F_0}{\partial t})_{\text{mix,max}} / ((\frac{\partial F_0}{\partial t})_{\perp,\text{max}}) \propto (I_2/I_1)^{-2}$. These values are calculated for a temperature of $\theta = 10^{-1}$.

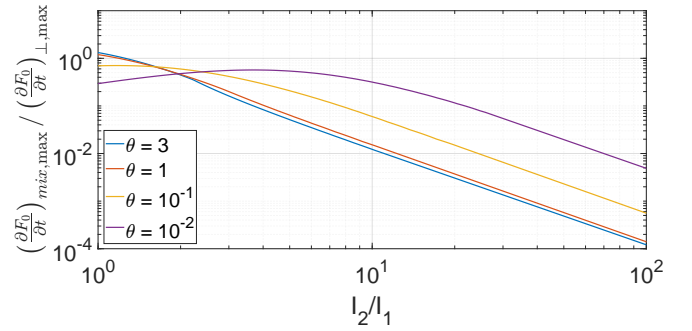


Figure 10. The ratio of the maximum value of the mixed term, $(\frac{\partial F_0}{\partial t})_{\text{mix,max}}$, to the maximum value of the perpendicular terms, $(\frac{\partial F_0}{\partial t})_{\perp,\text{max}}$, plotted versus I_2/I_1 . Each line represents a different temperature, with the peak of the ratio not at $I_2/I_1 = 1$ for $\theta = 10^{-2}$, as discussed in Section 4.

$(\frac{\partial F_0}{\partial t})_{\text{mix,max}} / (\frac{\partial F_0}{\partial t})_{\perp,\text{max}} \propto \sigma_{\text{rel}}$ trend at low magnetizations as described above. The region where the ratio flattens out, namely $I_2/I_1 \lesssim 2 - 10$ (depending on the temperature), corresponds to a much larger region in terms of the magnetization due to the asymptotic behaviour of the $I_2/I_1 - \sigma$ relationship as the relativistic Alfvén velocity approaches the speed of light. This results in the relatively broader non-power law regions in Fig. 11 compared to Fig. 10. These trends are reproduced in the numerical results for f_{inv} presented below in Section 4, supporting our conclusion about the importance of the mixed term.

4 RESULTS

4.1 The energy in the population inversion

Fig. 12a to 12d show the fraction of energy in the population inversion, f_{inv} versus σ_{rel} for temperatures of $\theta = \{3, 1, 10^{-1}, 10^{-2}\}$ respectively. All the results below are presented in terms of σ_{rel} rather than I_2/I_1 as the magnetization is a more useful physical quantity. These results show that the behaviour of f_{inv} with respect to the magnetization of the

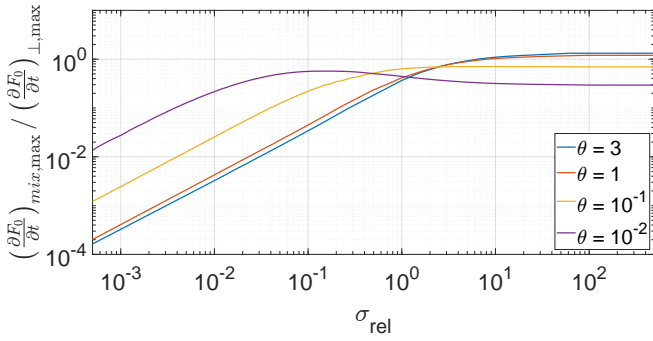


Figure 11. The ratio of the maximum value of the mixed term, $\left(\frac{\partial F_0}{\partial t}\right)_{mix,max}$, to the maximum value of the perpendicular terms, $\left(\frac{\partial F_0}{\partial t}\right)_{\perp,max}$, plotted versus the relativistic magnetization σ_{rel} . Note the broadness of the region where $\left(\frac{\partial F_0}{\partial t}\right)_{mix,max} / \left(\frac{\partial F_0}{\partial t}\right)_{\perp,max}$ is not proportional to σ_{rel} in comparison to the equivalent region in Fig. 10, caused by the asymptotic behaviour of σ as a function of I_2/I_1 for $\sigma > 1$.

plasma can be divided up into three regimes. These consist of a high magnetization regime where f_{inv} is only weakly dependent on σ_{rel} , an intermediate magnetization regime where $f_{inv} \propto \sigma_{rel}$, and a low magnetization regime where f_{inv} decreases rapidly as the magnetization decreases. These regimes and their properties are discussed in detail below, and a summary of the different regimes is given in Table 1.

The transition between the high and intermediate magnetization regimes occurs at a $\sigma_{rel} = \sigma_1$. We define this value as the maximum magnetization for which $f_{inv} \propto \sigma_{rel}$. Above this value, the fraction of energy in the population inversion depends weakly on the magnetization, as can be seen by the flattening out of f_{inv} for $\sigma_{rel} > \sigma_1$ in Fig. 12a to 12d. We note that this transition is not a sharp cut-off at precisely σ_1 , but a more gradual change, as can be seen in both the numerical results (Fig. 12a to 12d) and the ratio of $\left(\frac{\partial F_0}{\partial t}\right)_{mix,max} / \left(\frac{\partial F_0}{\partial t}\right)_{\perp,max}$ (Fig. 10 and 11). As discussed in Section 3.2, the relative strength of the mixed term is important to the formation of the population inversion. Indeed, the trend of f_{inv} can be explained by the similar behaviour of $\left(\frac{\partial F_0}{\partial t}\right)_{mix,max} / \left(\frac{\partial F_0}{\partial t}\right)_{\perp,max}$ in the same magnetization regime, as shown in Fig. 11.

While for higher temperatures of $\theta > 10^{-1}$ the fraction of energy in the inversion simply transitions to an asymptotic value for $\sigma_{rel} > \sigma_1$, this is not the case for $\theta = 10^{-2}$ (see Fig. 12d). At this lower temperature, both f_{inv} and $\left(\frac{\partial F_0}{\partial t}\right)_{mix,max} / \left(\frac{\partial F_0}{\partial t}\right)_{\perp,max}$ initially increase with σ_{rel} until reaching a peak value at σ_{peak} . This magnetization corresponds to the value at which the inversion contains the highest energy fraction for a given temperature. However, f_{inv} then decreases as σ_{rel} increases up to σ_0 , which we define as the magnetization at which $I_2/I_1 = 1$. As discussed in Section 2.1, this value is obtained when $v_{A,rel} \rightarrow c$. The change in behaviour at lower temperatures can be explained by noting that at σ_0 , the direction of $\left(\frac{\partial F_0}{\partial t}\right)_{max}$ is almost exactly perpendicular for $\theta = 10^{-2}$, as is shown in Fig. 6. This is not the most efficient angle for the formation of the crescent shape, as particles need to be accelerated to larger values of $|q_{\perp}|$ in the region $q_{\parallel} > 0$, rather than in the region centred at $q_{\parallel} = 0$.

Table 1. A summary of the relationship between f_{inv} and σ_{rel} in the different magnetization regimes

magnetization	f_{inv}
$\sigma_0 < \sigma_{rel}$	Constant
$\sigma_1 < \sigma_{rel} < \sigma_0$	Weakly dependent on σ_{rel}
$\sigma_2 < \sigma_{rel} < \sigma_1$	$f_{inv} \propto \sigma_{rel}$
$\sigma_{rel} < \sigma_2$	Decreases sharply as σ_{rel} decreases

When the magnetization $\sigma_{rel} > \sigma_0$, the ratios of the various terms in equation (3) are constant because I_1 , I_2 and I_3 are unchanging. Therefore, the fraction of energy in the inversion is independent of σ_{rel} when $\sigma_{rel} > \sigma_0$. This region is shown by the horizontal blue bars in Fig. 12a to 12d, which continue indefinitely to higher values of σ_{rel} . For temperatures of $\theta \geq 10^{-1}$, σ_0 also corresponds to σ_{peak} , as the ratio $\left(\frac{\partial F_0}{\partial t}\right)_{mix,max} / \left(\frac{\partial F_0}{\partial t}\right)_{\perp,max}$ is at its greatest for $I_2/I_1 = 1$. Therefore, for these temperatures f_{inv} is at its maximum value for all $\sigma_{rel} \geq \sigma_0$.

Below σ_1 , the plasma is in the intermediate magnetization region where the fraction of energy in the population inversion increases linearly with σ_{rel} . As in the high magnetization regime, this behaviour can be explained by the relative strength of the mixed term, as $\left(\frac{\partial F_0}{\partial t}\right)_{mix,max} / \left(\frac{\partial F_0}{\partial t}\right)_{\perp,max}$ is also proportional to σ_{rel} for $\sigma_{rel} < \sigma_1$. This reduction in f_{inv} corresponds to the weakening of the pitch angle diffusion as the magnetization decreases (and plasma β increases), as discussed in Section 3.3. In this regime the crescent shape no longer forms as clearly as in the high magnetization regime, as can be seen by comparing Fig. 5c, which shows $\frac{\partial F_0}{\partial t}$ in this intermediate magnetization regime, to Fig. 5a and 5b which have $\sigma_{rel} > \sigma_1$.

The $f_{inv} \propto \sigma_{rel}$ relationship holds for all $\sigma_1 > \sigma_{rel} > \sigma_2$. Here, σ_2 is the magnetization value below which a cut-off exists. This effect occurs due to the appearance of a positive region of $\frac{\partial F}{\partial t}$ centred at $q_{\perp} = 0$ and $q_{\parallel} < 0$ once the magnetization drops below this cut-off value. Above this threshold there is little to no diffusion in the parallel direction, with particles rather being moved to larger positive q_{\parallel} values only. However, below σ_2 , particles begin to spread in both the positive and negative q_{\parallel} direction, sharply reducing the fraction of particles being added to the population inversion. The contrast in $\frac{\partial F}{\partial t}$ between the two scenarios is visible by comparing Fig. 5d, which presents $\frac{\partial F}{\partial t}$ for $A = 1$, to Fig. 13, which shows $\frac{\partial F}{\partial t}$ for $A = 1.1$. $I_2/I_1 = 30$ and $\theta = 10^{-1}$ in both cases. In order for this effect to occur, a temperature anisotropy with $\theta_{\perp} > \theta_{\parallel}$ is required, as is shown below. Such an anisotropy always occurs due to the nonresonant interaction (Wang et al. 2006), and the cut-off effect acts to reduce this anisotropy by increasing θ_{\parallel} . As discussed in Section 3.3, the strength of A depends on both the magnetization and temperature. For the low magnetization regime in question here, the temperature anisotropy is generally small, with $1 \lesssim A < 2$.

An approximation for the value of σ_2 can be found by determining when $\frac{\partial F}{\partial t}$ first becomes positive for $q_{\perp} = 0$ and $q_{\parallel} < 0$. For the purpose of the following analysis, we assume an anisotropic Maxwell-Jüttner distribution of the form (Baumjohann & Treumann 2023)

$$F = C \exp\left(-\theta_{\perp}^{-1} \sqrt{1 + q_{\perp}^2 + A q_{\parallel}^2}\right), \quad (15)$$

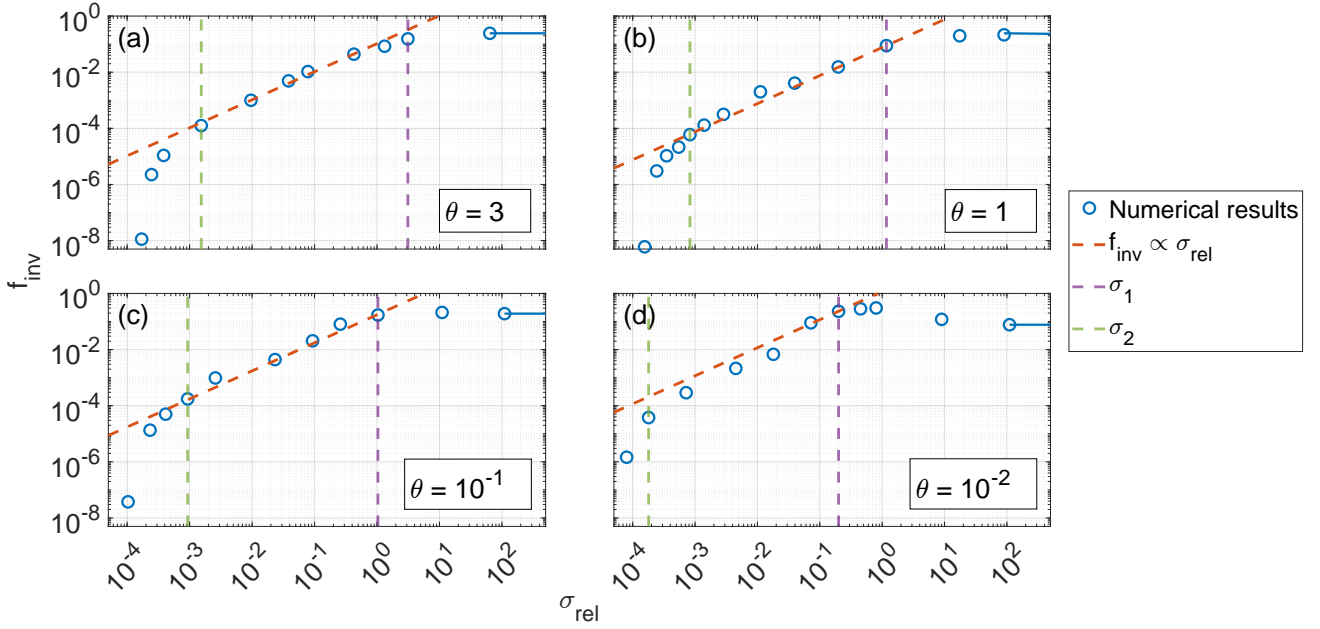


Figure 12. The energy in the inversion versus magnetization, with different temperatures in each panel. **Panel (a)** presents results for $\theta = 3$, **panel (b)** for $\theta = 1$, **panel (c)** for $\theta = 10^{-1}$ and **panel (d)** shows results for $\theta = 10^{-2}$. In each panel the purple dashed line (σ_1) divides the high and intermediate magnetization regime, and the green dashed line (σ_2) is the boundary between the low and intermediate magnetization regimes, showing where the cut-off occurs. The dashed orange line shows a fit of $f_{inv} \propto \sigma_{rel}$ in the intermediate magnetization regime in each case.

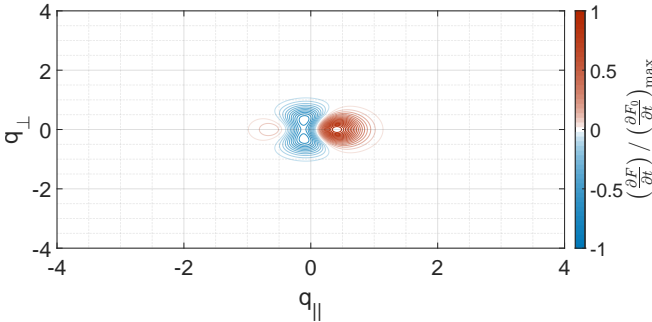


Figure 13. Contour plot of $\frac{\partial F}{\partial t}$ for an anisotropic Maxwell-Jüttner distribution in the low magnetization regime with $\theta = 0.1$, $I_2/I_1 = 30$ and $A = 1.1$. Note the appearance of the positive region of $\frac{\partial F}{\partial t}$ centred at $q_{\perp} = 0$ for $q_{\parallel} < 0$, which is completely absent when no temperature anisotropy is present.

where C is the normalization factor. While this does not capture the full crescent shape expected at high magnetizations, it is a good approximation for low magnetizations where the fraction of particles in the inverted population is small. The expression for $\frac{\partial F(q_{\perp}=0)}{\partial t}$ is taken from Eq. 3:

$$\begin{aligned} \frac{\partial F(q_{\perp}=0)}{\partial t} = & -C \frac{\exp\left(-\theta_{\perp}^{-1} \sqrt{1 + Aq_{\parallel}^2}\right)}{\theta_{\perp} (1 + q_{\parallel}^2)^{3/2} \sqrt{1 + Aq_{\parallel}^2}} \\ & \times \left(-(A-1)I_2 q_{\parallel}^2 \sqrt{1 + q_{\parallel}^2} + (A-2)I_1 q_{\parallel} (1 + q_{\parallel}^2) \right. \\ & \left. + I_3 (1 + q_{\parallel}^2)^{3/2} \right), \end{aligned} \quad (16)$$

where C contains all the constants omitted for clarity. Setting

$\frac{\partial F(q_{\perp}=0)}{\partial t} = 0$ results in the expression

$$-(A-1)I_2 q_{\parallel}^2 \sqrt{1 + q_{\parallel}^2} + (A-2)I_1 q_{\parallel} (1 + q_{\parallel}^2) + I_3 (1 + q_{\parallel}^2)^{3/2} = 0. \quad (17)$$

The solution for $q_{\parallel} < 0$ in the linear regime where $I_1 = \frac{v_{A,rel}}{c} I_2 = \frac{c}{v_{A,rel}} I_3$ is then given by

$$q_{\parallel} = -\frac{1}{\sqrt{(I_2/I_1)^2 (A-1)^2 - 1}}. \quad (18)$$

A positive $\frac{\partial F}{\partial t}$ in the $q_{\parallel} < 0$ region is only possible when $I_2/I_1 > 1/|A-1|$. As I_2/I_1 increases, the required anisotropy becomes smaller. In other words, this effect occurs sooner for lower magnetizations, resulting in the lower values of f_{inv} as σ_{rel} decreases. This relationship is only weakly dependent on the temperature, with the only effect occurring as a result of the temperature dependence of the $\sigma - I_2/I_1$ relationship, as shown in Fig. 1. The maximum value of σ_{rel} for which a positive $\frac{\partial F}{\partial t}$ in the $q_{\parallel} < 0$ region will appear is plotted in Fig. 14 as a function of the temperature anisotropy. The figure extends only to $\sigma_{rel} = 10^2$ as this is the approximate value at which $I_2/I_1 \rightarrow 1$. At low magnetizations the cut-off effect occurs for any anisotropy $A > 1$. The effect will therefore have an impact on the evolution of the distribution almost immediately. The needed anisotropy increases as the magnetization increases, with $A = 2$ required for $\sigma_{rel} > \sigma_0$ (equivalent to $I_2/I_1 = 1$). This result means that the positive $\frac{\partial F}{\partial t}$ in the $q_{\parallel} < 0$ region will appear for all parameters provided a sufficient temperature anisotropy exists, though in the high magnetization cases the crescent shape will have already largely formed before this occurs. The weak temperature dependence is also apparent in Fig. 14, with only a factor of ~ 2 in difference in the values of σ_{rel} for $\theta = 10^{-2}$ and $\theta = 3$. This result can also be seen in our numerical results,

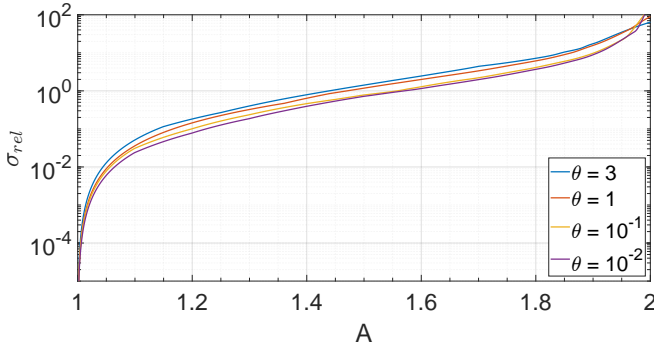


Figure 14. The maximum value of σ_{rel} for which a positive $\frac{\partial F}{\partial t}$ in the $q_{\parallel} < 0$ region will appear, plotted as a function of the temperature anisotropy A . A value of $\sigma_{rel} \sim 10^2$ corresponds to $I_2/I_1 = 1$. It can be seen that as the magnetization increases, the required anisotropy A for the cut-off effect to occur also increases from a value of $A \sim 1$ for $\sigma_{rel} \lesssim 10^{-4}$ to $A \sim 2$ for $\sigma_{rel} \sim 10^2$. The relationship depends only weakly on the temperature, with the effect becoming relevant for very small temperature anisotropies of close to 1 at low magnetizations in all cases.

where σ_2 only varies weakly between temperatures. However, we note that the values of σ_2 shown in Fig. 12a to 12d are only approximations due to the transition region not being sharp.

To examine the temperature dependence of f_{inv} , we plot all the results from Fig. 12a to 12d together in Fig. 15, which shows f_{inv} for every parameter set examined. Firstly, examining the results for $\sigma_{rel} > \sigma_0$ shows only a weak temperature dependence for $\theta = 10^{-1}$ to $\theta = 3$, with $f_{inv} \sim 0.2$ for these temperatures. The energy fraction for $\theta = 10^{-2}$ is lower at $f_{inv} \sim 0.08$. This matches the results presented in Fig. 11, with the peak energy for $\theta = 10^{-2}$ occurring at $\sigma_{rel} \sim 1$ rather than σ_0 . All maximum values are within the range $0.2 < f_{inv} < 0.3$, again matching predictions as there is no major difference between the peak values of $(\frac{\partial F_0}{\partial t})_{mix,max} / (\frac{\partial F_0}{\partial t})_{\perp,max}$ for different temperatures. The relative similarity of these results despite the range of temperatures examined spanning over 2 orders of magnitude shows that in the high magnetization regime the nonresonant interaction is capable of producing a substantial population inversion across a wide range of both relativistic and non-relativistic temperatures.

In the low and intermediate magnetization regimes the temperature dependence of the results is more pronounced, as can be seen by examining the region $\sigma_{rel} \lesssim 1$ in Fig. 15. The general increase in σ_2 with temperature, though slight, is visible. Furthermore, for a given σ_{rel} , f_{inv} increases as the temperature decreases, with a typical difference of over an order of magnitude between results for $\theta = 3$ and $\theta = 10^{-2}$. This indicates that the mechanism becomes less efficient in the relativistic regime at low magnetizations. As discussed in Section 3.3, this is due to the decrease in relative strength of the pitch angle diffusion at higher temperatures. The weaker contribution from the mixed term at higher temperatures can be seen in Fig. 10 and 11, as the relative strength of the mixed term for a given magnetization decreases as the temperature increases. The general decrease in f_{inv} for lower magnetizations leads us to conclude that the parameter space $\sigma_{rel} > \sigma_1$ is the one of most relevance to SME, as here $f_{inv} \gtrsim 10^{-1}$ for

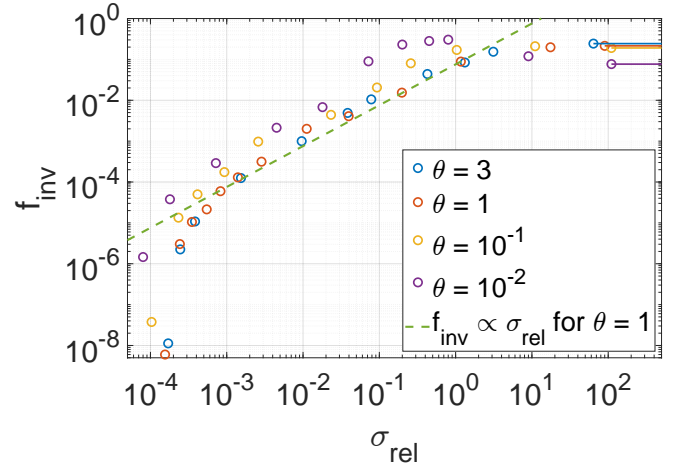


Figure 15. The energy in the inversion versus magnetization for $\theta = 10^{-2}$ to $\theta = 3$. The green dashed line shows a fit of $f_{inv} \propto \sigma_{rel}$ in the intermediate magnetization regime for $\theta = 1$. In the low- and intermediate- σ_{rel} regimes f_{inv} generally decreases as the temperature increases.

all temperatures and a clear crescent shape is always formed as $\alpha > 0$.

4.2 Time-scales

The time taken for the population inversion to form is another important result as the mechanism must operate on a time-scale shorter than the characteristic dynamical time-scale to provide a valid explanation for FRBs. Fig. 16a to 16d show the time taken to reach the asymptotic value of f_{inv} for all the results presented above, i.e. spanning the parameter space $10^{-4} < \sigma_{rel}$ and $10^{-2} < \theta < 3$. The results are presented in units of $(\Omega_0 \Gamma \eta)^{-1}$ s, as the typical observed frequency of FRBs is ~ 1 GHz (e.g. Petroff et al. 2022). As the fraction of energy in the population inversion for a given parameter set approaches its asymptotic maximum value f_{inv} , the rate at which the fraction increases decreases, making the time taken to reach the maximum value difficult to precisely define. Therefore in order to present the results more clearly, Fig. 16a to 16d below present the time taken to reach $0.9f_{inv}$ for each parameter set, with the lower error bar showing the time to reach $0.1f_{inv}$ and the upper error bar showing the time at which final asymptotic value f_{inv} was obtained. All the time-scale results presented below are for a wavenumber range of $0 < k < 0.01\Omega/c$ and a flat Alfvén wave spectrum. The equivalent time-scales for other spectra can be retrieved using equation (11) as described in Section 2.2.

For all temperatures, the behaviour as a function of σ_{rel} in the high- σ_{rel} and intermediate- σ_{rel} regimes is similar to the results for f_{inv} . The time taken for the inversion to form increases approximately linearly with respect to σ_{rel} before beginning to asymptote for $\sigma_{rel} > \sigma_1$. This indicates that the rate at which the inversion is formed is approximately constant in these regimes. This behaviour changes in the low- σ_{rel} regime below σ_2 . While f_{inv} sharply drops off, the time taken to reach this asymptotic value does not display a similar reduction. It instead deviates only slightly from the same linear relationship as the intermediate magnetization region. This can be explained by the fact that the formation of the cres-

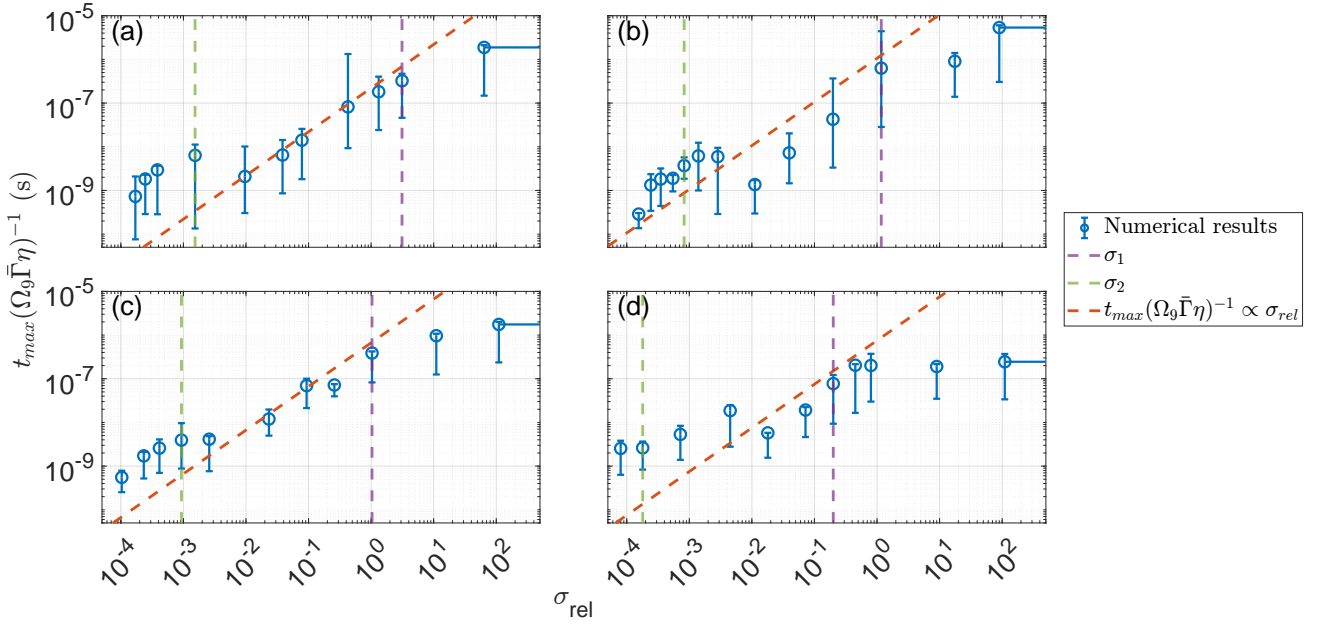


Figure 16. Plot of t_{max} in time units of $(\Omega_9 \bar{\Gamma} \eta)^{-1}$ s versus σ_{rel} , with different temperatures in each panel. **Panel (a)** presents results for $\theta = 3$, **panel (b)** for $\theta = 1$, **panel (c)** for $\theta = 10^{-1}$ and **panel (d)** shows results for $\theta = 10^{-2}$. In each case the purple dashed line (σ_1) shows the transition point between the high and intermediate magnetization regimes, while the green dashed line (σ_2) is the boundary between the low and intermediate magnetization regimes, showing where the cut-off occurs.

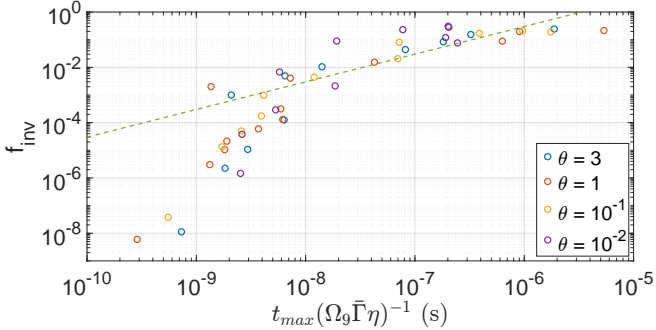


Figure 17. Plot of the asymptotic fraction of energy in the inversion versus t_{max} in time units of $(\Omega_9 \bar{\Gamma} \eta)^{-1}$ s for various temperatures. The dashed green line shows $f_{inv} \propto t_{max}$ for the intermediate magnetization regime.

cent shape has become much less efficient due to the impact of the positive $\frac{\partial F}{\partial t}$ for $q_{||} < 0$, as discussed in detail above. In other words, both the rate at which the inversion forms and the maximum achievable f_{inv} are sharply reduced in this regime. This result can also be seen in Fig. 17 where f_{inv} is plotted versus t_{max} . In this figure, and in Fig. 18a and 18b below the error bars have been omitted to make the plots more readable. The dashed green line shows the linear region $f_{inv} \propto t_{max}$, and the low magnetization regime is shown by the sharp decrease in f_{inv} at shorter time-scales.

As can be seen in Fig. 16, at low magnetizations the times become as short as $t_{max} \sim 10^{-9} (\Omega_9 \bar{\Gamma} \eta)^{-1}$ s for all temperatures. At higher magnetizations the time-scales become longer, increasing to asymptotic values for $\sigma_{rel} > \sigma_0$ ranging from $t_{max} \sim 2 \times 10^{-7} (\Omega_9 \bar{\Gamma} \eta)^{-1}$ s for $\theta = 10^{-2}$ to $t_{max} \sim 5 \times 10^{-6} (\Omega_9 \bar{\Gamma} \eta)^{-1}$ s for $\theta = 1$. In contrast to the high magnetization regime, the results in both Fig. 16 and 17 do

not show any strong temperature dependence in the low and intermediate magnetization regimes, with time-scales changing by a factor of only a few across the full range of temperatures investigated in the low and intermediate magnetization regimes. The time-scale results presented here are compared to the relevant magnetar time-scales in Section 5.2.

5 DISCUSSION

5.1 SME efficiency and other plasma instabilities

The numerical results presented in Section 4 above demonstrate that energy fractions of up to $f_{inv} \sim 0.3$ are attainable at high magnetizations through the nonresonant interaction between Alfvén waves and relativistic plasma. The energy fraction decreases linearly with σ_{rel} in the intermediate regime $\sigma_2 < \sigma_{rel} < \sigma_1$ before dropping sharply below the cut-off σ_2 . The time-scale in all cases is $t_{max} \lesssim 5 \times 10^{-6} (\Omega_9 \bar{\Gamma} \eta)^{-1}$ s, with this value decreasing approximately linearly with σ_{rel} for $\sigma_1 < \sigma_{rel} < \sigma_2$. The above results are only weakly dependent on the temperature, with at most an order of magnitude difference in f_{inv} between $\theta = 10^{-2}$ and $\theta = 3$ in the low and intermediate magnetization regimes. We discuss the applicability of these parameters to magnetars and other neutron stars in Section 5.3, as these are the leading candidates for FRB progenitors, with one FRB directly observed to have originated from the galactic magnetar SGR 1935+2154 (CHIME/FRB Collaboration et al. 2020).

The results for f_{inv} summarized above and presented in detail in Section 4.1 can be contrasted with the efficiency results obtained from PIC simulations of relativistic shocks, another important candidate in explaining SME in relativistic environments (e.g. Gallant et al. 1992; Amato & Arons 2006; Plotnikov & Sironi 2019). In the relativistic shock model,

the population inversion is not formed through nonresonant interactions with Alfvén wave. Instead, a soliton-like structure forms at the front of a shock with high magnetization. In this structure, the particles gyrating around the enhanced magnetic field near the shock front form a semi-coherent ring-like distribution in momentum space which can support SME (e.g. [Alsop & Arons 1988](#); [Gallant et al. 1992](#); [Amato & Arons 2006](#); [Plotnikov & Sironi 2019](#)).

Comparing the results obtained for f_{inv} from the nonresonant interaction to the efficiency values from the relativistic shock model shows several differences in the viable parameter spaces. In the high magnetization regime, the results presented above in Section 4 produce considerably higher f_{inv} than in the case of relativistic shocks, where an efficiency of $\sim 10^{-3}\sigma_{rel}^{-1}$ for $\sigma_{rel} \gg 1$ was found ([Sironi et al. 2021](#)). On the other hand, in the intermediate magnetization regime, for a magnetization of $\sigma_{rel} \sim 0.1$ the shock efficiency was found to be ~ 0.1 ([Plotnikov & Sironi 2019](#)), comparable to the values found in this work for $\theta > 10^{-2}$. These are approximately $f_{inv} \sim 10^{-1}\sigma_{rel}$ for $\sigma_2 < \sigma_{rel} < 1$ for $\theta = 10^{-1}$ to $\theta = 3$, and $f_{inv} \sim \sigma_{rel}$ for $\sigma_2 < \sigma_{rel} < 0.1$ for $\theta = 10^{-2}$. These results suggest that nonresonant interactions with Alfvén waves may be the more viable mechanism at high magnetizations, while relativistic shocks, if exist, may be more relevant at lower magnetizations.

We emphasize that the efficiency in the relativistic shock scenario and f_{inv} are not the same quantity. While the efficiency values above describe the fraction of energy actually emitted by SME, f_{inv} provides an upper limit on the total energy fraction available from the deformed distribution. Not all of this energy will necessarily be extracted due to the influence of other plasma processes. For instance, at higher temperatures the SME growth rate may be reduced ([Amato & Arons 2006](#); [Iwamoto et al. 2017](#); [Babul & Sironi 2020](#)). This, though, may not affect the overall efficiency, provided that all other plasma instabilities will have a slower growth rate.

The impact of plasma instabilities is most relevant for the high temperature and low magnetization regions of the parameter space. As noted above, the particle distribution can be roughly approximated as a Bi-Maxwellian, especially in the low magnetization regime where the fraction of energy in the inversion is small. In such distributions both the firehose and mirror instabilities are important. These have stability criteria of $A > 1 - 1/\beta_{\parallel}$ for the firehose instability and $A < 1 + 1/\beta_{\parallel}$ for the mirror instability ([Gary 1993](#)). Here $\beta_{\parallel} = 2\theta_{\parallel}/\sigma_{rel}$ is the parallel plasma beta. When $\sigma_{rel} \gg 1$, $\beta_{\parallel} \ll 1$ for all temperatures, resulting in a distribution which is not susceptible to either of the instabilities. However, when $\sigma_{rel} \ll 1$ and the temperature is relativistic, even a small temperature anisotropy will result in the stability criteria no longer being satisfied. In the case of the low magnetization regime, the temperature anisotropy is typically in the range $1 \lesssim A \lesssim 2$, and so the distribution will be potentially affected by the mirror instability at high temperatures. This means that plasmas in the low and intermediate magnetization regimes have both lower energy fractions and are more susceptible to instabilities. On the other hand, this issue has no effect on the most efficient parameters, namely those in the high magnetization regime, strengthening the conclusion that this is the regime of most relevance for SME in astrophysical scenarios.

5.2 Magnetar time-scales

As magnetars are the primary candidate for FRB progenitors ([CHIME/FRB Collaboration et al. 2020](#)), we consider the typical time-scales of such objects. Magnetars have two time-scales of interest, namely the radius and period of the star, either of which could potentially provide the crucial time variability in the Alfvén wave field which is a requirement for a nonresonant interaction. Firstly, the magnetar radius R_* corresponds to a time-scale of $\sim R_*/c = 3.3 \times 10^{-5} R_{*,6}$ s. The time-scale of the magnetar rotational period is significantly longer, typically $\sim 1 - 10$ s ([Mereghetti 2008](#); [Olausen & Kaspi 2014](#)),³ though young magnetars may have millisecond periods ([Dall’Osso & Stella 2022](#)).

In [Fig. 18a](#) and [18b](#) we show the minimum allowed values of $\bar{\Gamma}\eta$ needed to satisfy the magnetar rotational period and radius time-scales respectively. In the period case, $P^{-1}\Omega_9(\bar{\Gamma}\eta)_{\min} \ll 1$ for all the magnetizations and temperatures studied. Therefore, this time-scale is compatible with our results for the whole parameter space, even if the magnetar period deviates substantially from $P \sim 1$ s. In contrast, the magnetar radius time-scale is much more constraining, with $R_{*,6}^{-1}\Omega_9(\bar{\Gamma}\eta)_{\min} > 10^{-2}$ for $\sigma_{rel} \gtrsim 1$, increasing to $\sim 10^{-1}$ for the high magnetization regime at relativistic temperatures. To satisfy these more stringent limits, the Alfvén waves need to be both relatively strong compared to the background magnetic field ($\eta \gtrsim 10^{-1}$), or to have a very high growth rate ($\bar{\Gamma} \gtrsim 10^{-1}$), suggesting it is a less likely model for providing the required conditions for the formation of a population inversion. As in [Section 4.2](#) the constraints on $(\bar{\Gamma}\eta)_{\min}$ presented here are for a wavenumber range of $0 < k < 0.01\Omega/c$ and a flat Alfvén wave spectrum. The equivalent constraints for other spectra can be calculated as detailed in [Section 2.2](#).

5.3 Physical scenarios for FRBs

As mentioned above, magnetars are the most likely progenitors of FRBs as they naturally provide the large energies and small size and time scales necessary to produce the high brightness temperatures observed from FRBs (e.g. [Zhang 2020](#)). FRB 200428 has also been observed to originate from the galactic magnetar SGR 1935+2154 ([CHIME/FRB Collaboration et al. 2020](#)). In our model, we assume that the required Alfvén waves for the nonresonant interaction are produced by a quake or similar instability of the central magnetar (e.g. [Blaes et al. 1989](#); [Beloborodov 2023b](#)). These waves propagate outwards before interacting with a relativistic plasma, with the resulting nonresonant interaction producing a population inversion and SME. In order for this to produce an FRB signal, the interaction must occur in a region of parameter space where a high value of f_{inv} can be achieved on a time-scale compatible with the dynamical time-scales discussed in [Section 5.2](#). The plasma parameters must also allow a peak SME frequency appropriate for FRBs, whose signals have primarily been detected in the GHz band with frequencies ranging from 110 MHz ([Fedorova & Rodin 2019](#); [Pleunis et al. 2021a](#); [Pastor-Marazuela et al. 2021](#)) to 8 GHz ([Gajjar et al. 2018](#)).

³ <https://www.physics.mcgill.ca/pulsar/magnetar/main.html>

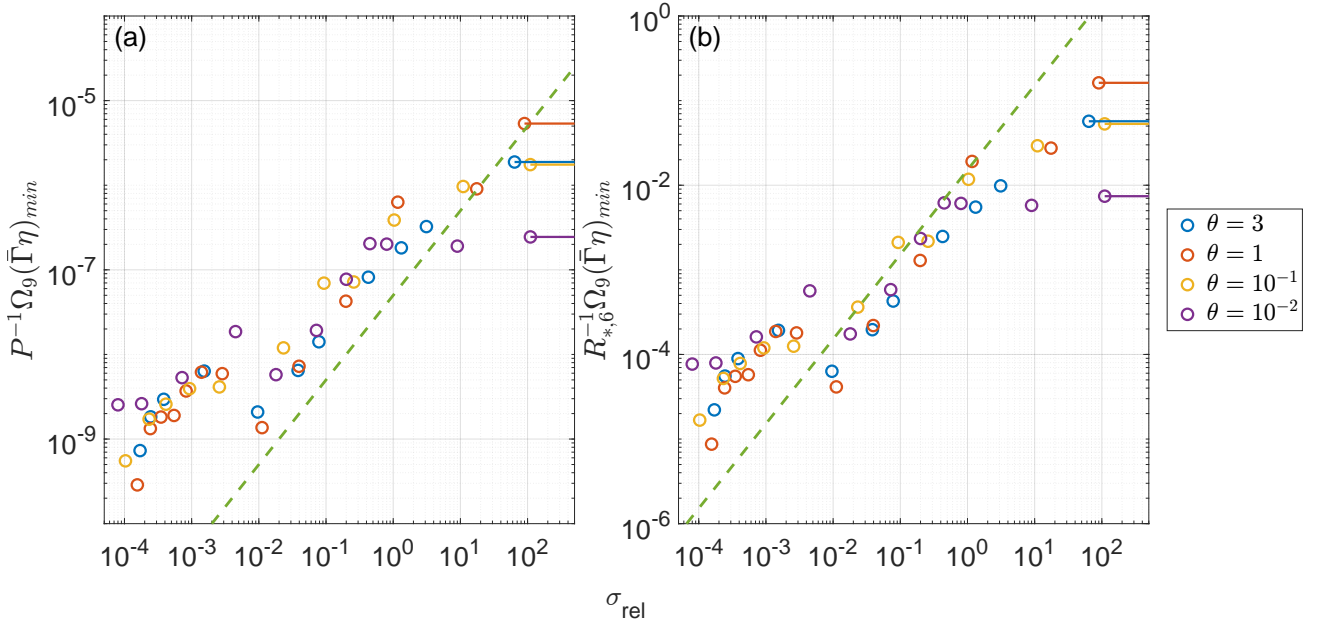


Figure 18. Plots of the constraints on $\bar{\Gamma}\eta$ for the magnetar period and radius time-scales. **Panel (a)** presents the minimum allowed value $P^{-1}\Omega_9(\bar{\Gamma}\eta)_{\min}$ that produces the population inversion in a time shorter than a neutron star period of $P = 10$ seconds. **Panel (b)** shows the minimum allowed value $R_{*,6}^{-1}\Omega_9(\bar{\Gamma}\eta)_{\min}$ that produces the population inversion in a time shorter than the neutron star radius time-scale of $\sim R_*/c = 3.3 \times 10^{-5}R_{*,6}$ s. In both panels different colors denote different temperatures, while the dashed green lines show linear fits of $P^{-1}\Omega_9(\bar{\Gamma}\eta)_{\min} \propto \sigma_{rel}$ and $R_{*,6}^{-1}\Omega_9(\bar{\Gamma}\eta)_{\min} \propto \sigma_{rel}$ respectively.

The plasma parameters required to achieve such SME frequencies depend on the magnetization of the plasma. At higher magnetizations of $\sigma_{rel} > 1$, the maser’s peak frequency is $\omega_m \sim \Omega\gamma_{av}^{-1}$ (Lyubarsky 2021). If the plasma where the emission occurs is moving towards the observer with Lorentz factor γ_B , this results in a required magnetic field of $B_0 \sim 360\nu_9\gamma_{av}\gamma_B^{-1}$ G. Here ν is the FRB frequency in Hz. In order to satisfy $\sigma_{rel} > 1$, the upper limit on the number density in this regime is $n_{\max} \sim 1.2 \times 10^{10}\nu_9^2\gamma_{av}\gamma_B^{-2}$ cm $^{-3}$. On the other hand, when $\sigma_{rel} < 1$, the peak frequency for SME occurs at $\omega_m \approx \gamma_{av}^{-1/2}\omega_{p\min}\{\gamma_{av}, \sigma_{rel}^{-1/4}\}$ (Sagiv & Waxman 2002). As ω_m is only very weakly dependent on the magnetization, the peak frequency will never be much higher than a few times $\gamma_{av}^{-1/2}\omega_p$. The number density required to produce emission at FRB frequencies is therefore $n \sim 1.2 \times 10^{10}\nu_9^2\gamma_{av}\gamma_B^{-2}\max\{\gamma_{av}^{-2}, \sigma_{rel}^{1/2}\}$ cm $^{-3}$, with a corresponding upper limit on the magnetic field of $B_{0,\max} \sim 360\nu_9\gamma_{av}\gamma_B^{-1}\max\{\gamma_{av}^{-1}, \sigma_{rel}^{1/4}\}$ G to satisfy $\sigma_{rel} < 1$. As the values for the magnetic field in the $\sigma_{rel} < 1$ case and the number density in the $\sigma_{rel} > 1$ case are both upper limits, a large parameter space is viable for SME.

As the high magnetization regime produces the largest values of f_{inv} and is less susceptible to plasma instabilities we first examine a model in this regime by considering Alfvén waves propagating through a relativistic magnetar wind. These winds have typical magnetizations of $\sigma_{wind} \sim 280B_{*,15}^{8/9}R_{*,6}^{24/9}M_3^{-2/3}P^{-2}$ outside the light cylinder radius $R_{LC} = cP/2\pi = 4.8 \times 10^9P$ cm (Lyubarsky 2021). Here B_* is the surface magnetic field and M is the pair multiplicity. This magnetization value is well above σ_1 for all temperatures, and so is in the high magnetization regime with a correspondingly high $f_{inv} \gtrsim 0.1$ at all tem-

peratures examined. Furthermore as f_{inv} is close to constant for all σ_{rel} in this regime, the precise magnetization value of the wind does not effect the validity of the mechanism provided that $\sigma_{wind} > \sigma_1$. The distance from the neutron star at which emission could occur in the FRB frequency range is $R_{FRB} \sim 1.2 \times 10^{11}\nu_9^{-1}\gamma_B\gamma_{av}^{-1}B_{*,15}R_{*,6}^3P^{-2}$ cm, assuming $B \propto 1/R$ outside the light cylinder. This means that maser emission in this scenario occurs just outside the magnetosphere at radii approximately an order of magnitude smaller than in relativistic shock models, depending on the precise parameters of the FRB in question (Margalit et al. 2020). As discussed above in Section 5.2 the high magnetization regime is restrictive in terms of the magnetar radius time-scale, especially at relativistic temperatures. This suggests that a longer scale such as the magnetar period is responsible for the variation in the Alfvén waves in this model. The particle number density at this distance is significantly below the upper limits for n_{\max} discussed above, so SME at the appropriate frequencies is viable in this scenario assuming the population inversion has successfully formed.

This model also implies that SME may occur at smaller radii and thus higher frequencies than those observed from FRBs, as the background magnetic field is larger closer to the magnetar. Inside the magnetosphere at $R < R_{LC}$, $\sigma_{rel} \gg 1$ and so a population inversion with a large energy fraction could possibly be formed. However in this region both $\eta = |E_k|^2/B_0^2$ and $\bar{\Gamma} = \Gamma/\Omega$ will be much smaller than at larger radii outside the light cylinder due to the extremely high $B_0 = 10^{15}B_{*,15}R_{*,6}^3/R_6^3$ G inside the magnetosphere. This will result in time-scales that are too long compared to the dynamical time-scales of the system for the mechanism to be practical.

Furthermore, strong radio emission may be damped due

to non-linear effects at radii similar to and smaller than those required in the relativistic magnetized wind scenario (Sobacchi et al. 2024b). This effect is important at $R \lesssim 2 \times 10^{12} L_{42}^{1/4} B_{*,15}^{1/2} P_{*,6}^{3/2} \nu_9^{-1} P^{-1}$ cm, where L is the FRB isotropic luminosity (which has been observed to vary from $L \sim 10^{36}$ erg s $^{-1}$ (Bochenek et al. 2020) to $L \sim 10^{46}$ erg s $^{-1}$ (Ravi et al. 2019; Ryder et al. 2023)). This constraint therefore requires $\gamma_B \gg 1$ to explain higher luminosity FRBs in the relativistic wind model. We note that the typical wind Lorentz factor is expected to be on the order of ~ 90 (Lyubarsky 2020a, 2021), satisfying this requirement. This constraint may also be weakened by the interaction of a flare from the original magnetar quake with the relativistic wind (e.g. Lyubarsky 2020b). SME at much lower frequencies than FRBs is also not feasible in this model as the Alfvén wave frequency becomes comparable to Ω at larger radii, violating the conditions required for the nonresonant interaction to be dominant as described in Section 2. The combination of these constraints leads us to conclude that nonresonant interaction between Alfvén waves and a relativistic magnetar wind leads to the appropriate conditions to produce FRBs at R_{FRB} . These limits may also provide information on the magnetar properties (such as period and magnetic field) based on the frequency and luminosity of observed FRB signals.

5.4 Alternative FRB scenarios

Magnetars may also be surrounded with a lower magnetization subrelativistic wind with $\beta_{wind} \lesssim 1$ and $\sigma_{wind} \lesssim 1$ (Metzger et al. 2019). Here $\beta_{wind} = v_{wind}/c$ is the normalized wind velocity. In this scenario wind densities of $n \sim 1.6 \times 10^5 \dot{M}_{21} R_{14}^{-2} \beta_{wind}^{-1}$ cm $^{-3}$ are expected. Here, \dot{M} is the mass loss rate, which is normalized to constraints obtained from FRB 121102, where $\dot{M} \sim 10^{19} - 10^{21}$ g s $^{-1}$ (Margalit & Metzger 2018). This environment satisfies the constraints for maser emission at a similar radius as the relativistic magnetar wind, $R_{FRB} \sim 3.7 \times 10^{11} \nu_9^{-1} \dot{M}_{21}^{1/2} \beta_{wind}^{-1/2} \gamma_B \gamma_{av}^{-1/2} \min\{\gamma_{av}, \sigma_{rel}^{-1/4}\}$ cm. This scenario is therefore also susceptible to the damping effect described above for high luminosity FRBs, as well as having considerably lower values of f_{inv} than in the high magnetization case, with $f_{inv} \sim 0.1 \sigma_{rel}$ before dropping precipitously for $\sigma_{rel} < \sigma_2$. On the other hand this case does have much shorter time-scales, 2 to 3 orders of magnitude shorter than the high magnetization scenario.

The contrast between these two scenarios highlights the trade-off between the time taken for the population inversion to form and the energy fraction it contains. This is especially important to FRBs as it is unclear if all sources repeat or not. While some studies show observational differences between apparent one-off bursts and repeaters (Pleunis et al. 2021b; Petroff et al. 2022), these one-off bursts may also be rarer, brighter events than other undetected signals from the same object (Kirsten et al. 2024). For potential one-off bursts, the time taken for the inversion to form is not a limiting factor. On the other hand, if most or all FRBs repeat, the inversion must form with times shorter than the typical time between bursts. While this model can not intrinsically produce time-scales as short as the ~ 60 ns observed from the fastest repeaters (Nimmo et al. 2022), the vast majority of FRBs repeat on much longer time-scales, typically on the order of

seconds or longer (Lanman et al. 2022; Hu & Huang 2023). Variability on a very short time scale ($< \mu$ s) may also be induced by the propagation of the FRB signal through a highly magnetized plasma, rather than as a result of the emission process itself (Sobacchi et al. 2024a). These factors therefore do not limit the model to the low-magnetization regime as shorter time-scales would, suggesting that it is still a viable potential explanation for the majority of FRBs.

Observations of rapidly varying polarization angles similar to pulsar emission have led to arguments in favour of a magnetospheric origin for FRBs (Mckinven et al. 2024; Niu et al. 2024). SME typically produces emission with a high degree of linear polarization due to the ordered magnetic field lines in the emission region (e.g. Plotnikov & Sironi 2019), and does not intrinsically result in changes in polarization angle. However, recent works on SME from relativistic shocks suggest rapid swings of polarization angle are possible even far from a neutron star (Iwamoto et al. 2024), and that proximity to the central engine is therefore not a requirement to match observations. As the polarization properties of FRBs are also subject to propagation effects this is an area which requires further examination.

Recent works have also suggested that magnetospheric models at shorter distances from the central engine are favoured over SME from longer distances due to limits obtained from scintillation measurements (Nimmo et al. 2024). In both physical scenarios presented above, the distances R_{FRB} are comparable to the upper limits of $R \sim 3 \times 10^{11}$ cm obtained from scintillation measurements of FRB 20221022A (Nimmo et al. 2024), thus not ruling out SME as an emission mechanism in these scenarios. Emission at larger radii as in the models presented in this work also avoids potential issues with the propagation of the FRB signal out of the magnetosphere, as radio waves may be strongly damped and struggle to escape (e.g. Beloborodov 2021; Golbraikh & Lyubarsky 2023; Beloborodov 2023a), though there is as of yet no consensus on this issue (e.g. Qu et al. 2022; Lyutikov 2024).

6 CONCLUSION

In this work, we showed that nonresonant interaction of Alfvén waves with a relativistic plasma produce population inversions for temperatures in the range $10^{-2} \leq \theta \leq 3$ and for magnetizations greater than $\sigma_{rel} \sim 10^{-4}$. We report that a significant fraction of the energy in the particle distribution is contained in the crescent shaped population inversion, with peak values of $f_{inv} \sim 0.3$ reached at magnetizations of $\sigma_{rel} \gtrsim 10$ for temperatures of $\theta \geq 10^{-1}$. At the lower temperature of $\theta = 10^{-2}$, the peak magnetization is lower at a value of $\sigma_{rel} \sim 0.1 - 1$, but similar energy fractions are obtained. In the intermediate magnetization regime with lower magnetizations of $\sigma_{rel} < \sigma_1 \sim 10^{-1}$ the energy fraction decreases as the magnetization decreases, with $f_{inv} \propto \sigma_{rel}$, before dropping sharply at a cut-off magnetization of $\sigma_{rel} = \sigma_2 \sim 10^{-4}$. The higher fractions of energy in the population inversion at high magnetizations across all temperatures, as well as reduced susceptibility to other instabilities, leads us to suggest that this regime is the most relevant for astrophysical scenarios such as FRBs.

The time-scale for the formation of the population inversion reaches its maximum value $t_{max} \lesssim 5 \times 10^{-6} (\Omega_9 \bar{\Gamma} \eta)^{-1}$ s

at high magnetizations, with this value decreasing approximately linearly with σ_{rel} for $\sigma_1 < \sigma_{rel} < \sigma_2$. These values are compatible with the magnetar period time-scale for all parameters, and with the magnetar radius time-scale at lower magnetizations. We have also demonstrated that the parameters at which the population inversion can form through nonresonant interactions are achievable in the environment of magnetars, and can lead to SME at the appropriate frequencies for FRBs. The FRB signal originates in the region close to but outside of the light cylinder, at distances of $R_{FRB} \sim 1.2 \times 10^{11} \nu_9^{-1} \gamma_B \gamma_{av}^{-1} B_{*,15} R_{*,6}^3 P^{-2}$ cm, and is able to escape the magnetar environment without significant damping.

ACKNOWLEDGEMENTS

AP acknowledges support from the European Union (EU) via ERC consolidator grant 773062 (O.M.J.). KL acknowledges the support of the Irish Research Council through grant number GOIPG/2017/1146 as well as funding obtained by the above ERC grant. The authors also wish to acknowledge the Irish Centre for High-End Computing (ICHEC) for the provision of computational facilities and support. We would also like to thank Antoine Bret for helpful discussions regarding plasma instabilities.

DATA AVAILABILITY

The code used to perform the calculations presented in this paper is available upon request.

REFERENCES

- Alsop D., Arons J., 1988, *Physics of Fluids*, **31**, 839
 Amato E., Arons J., 2006, *ApJ*, **653**, 325
 Asenjo F. A., Muoz V., Valdivia J. A., Hada T., 2009, *Physics of Plasmas*, **16**
 Babul A.-N., Sironi L., 2020, *MNRAS*, **499**, 2884
 Baumjohann W., Treumann R. A., 2023, *Frontiers in Physics*, **11**, 1174557
 Begelman M. C., Ergun R. E., Rees M. J., 2005, *ApJ*, **625**, 51
 Beloborodov A. M., 2020, *ApJ*, **896**, 142
 Beloborodov A. M., 2021, *ApJ*, **922**, L7
 Beloborodov A. M., 2023a, *arXiv e-prints*, p. arXiv:2307.12182
 Beloborodov A. M., 2023b, *ApJ*, **959**, 34
 Bilbao P. J., Silva L. O., 2023, *Phys. Rev. Lett.*, **130**, 165101
 Bilbao P. J., Silva T., Silva L. O., 2024a, *arXiv e-prints*, p. arXiv:2409.18955
 Bilbao P. J., Ewart R. J., Assunção F., Silva T., Silva L. O., 2024b, *Physics of Plasmas*, **31**, 052112
 Blaes O., Blandford R., Goldreich P., Madau P., 1989, *ApJ*, **343**, 839
 Bochenek C. D., Ravi V., Belov K. V., Hallinan G., Kocz J., Kulkarni S. R., McKenna D. L., 2020, *Nature*, **587**, 59
 CHIME/FRB Collaboration et al., 2020, *Nature*, **587**, 54
 Dall’Osso S., Stella L., 2022, in Bhattacharyya S., Papitto A., Bhattacharya D., eds, *Astrophysics and Space Science Library* Vol. 465, *Astrophysics and Space Science Library*. pp 245–280 (arXiv:2103.10878), doi:10.1007/978-3-030-85198-9_8
 Drummond W. E., Rosenbluth M. N., 1962, *The Physics of Fluids*, **5**, 1507
 Fedorova V. A., Rodin A. E., 2019, *Astronomy Reports*, **63**, 39
 Freund H. P., Wu C. S., 1976, *Physics of Fluids*, **19**, 299
 Gajjar V., et al., 2018, *ApJ*, **863**, 2
 Gallant Y. A., Hoshino M., Langdon A. B., Arons J., Max C. E., 1992, *ApJ*, **391**, 73
 Gary S. P., 1993, *Theory of Space Plasma Microinstabilities*. Cambridge University Press
 Golbraikh E., Lyubarsky Y., 2023, *ApJ*, **957**, 102
 Hewitt R. G., Melrose D. B., Ronnmark K. G., 1982, *Australian Journal of Physics*, **35**, 447
 Hu C.-R., Huang Y.-F., 2023, *ApJS*, **269**, 17
 Iwamoto M., Amano T., Hoshino M., Matsumoto Y., 2017, *ApJ*, **840**, 52
 Iwamoto M., Matsumoto Y., Amano T., Matsukiyo S., Hoshino M., 2024, *Phys. Rev. Lett.*, **132**, 035201
 Katz J. L., 2016, *Modern Physics Letters A*, **31**, 1630013
 Kirsten F., et al., 2024, *Nature Astronomy*, **8**, 337
 Lanman A. E., et al., 2022, *ApJ*, **927**, 59
 Long K., Pe’er A., 2018, *ApJ*, **864**, L12
 Long K., Pe’er A., 2023, *Phys. Rev. D*, **107**, L121301
 Lyubarsky Y., 2014, *MNRAS*, **442**
 Lyubarsky Y., 2020a, *ApJ*, **897**
 Lyubarsky Y., 2020b, *ApJ*, **897**, 1
 Lyubarsky Y., 2021, *Universe*, **7**
 Lyutikov M., 2024, *MNRAS*, **529**, 2180
 Margalit B., Metzger B. D., 2018, *ApJ*, **868**, L4
 Margalit B., Metzger B. D., Sironi L., 2020, *MNRAS*, **494**, 4627
 Mckinven R., et al., 2024, *arXiv e-prints*, p. arXiv:2402.09304
 Mereghetti S., 2008, *Astronomy and Astrophysics Review*, **15**, 225
 Metzger B. D., Margalit B., Sironi L., 2019, *MNRAS*, **485**
 Muñoz V., Asenjo F. A., Domínguez M., López R. A., Valdivia J. A., Viñas A., Hada T., 2014, *Nonlinear Processes in Geophysics*, **21**
 Nimmo K., et al., 2022, *Nature Astronomy*, **6**, 393
 Nimmo K., et al., 2024, *arXiv e-prints*, p. arXiv:2406.11053
 Niu J. R., et al., 2024, *ApJ*, **972**, L20
 Olausen S. A., Kaspi V. M., 2014, *ApJS*, **212**, 6
 Pastor-Marazuela I., et al., 2021, *Nature*, **596**, 505
 Petroff E., Hessels J. W. T., Lorimer D. R., 2022, *A&ARv*, **30**, 2
 Platts E., Weltman A., Walters A., Tendulkar S. P., Gordin J. E. B., Kandhai S., 2019, *Phys. Rep.*, **821**, 1
 Pleunis Z., et al., 2021a, *ApJ*, **911**, L3
 Pleunis Z., et al., 2021b, *ApJ*, **923**, 1
 Plotnikov I., Sironi L., 2019, *MNRAS*, **485**
 Press W. H., Teukolsky S. A., Vetterling W. T., Flannery B. P., 2007, *NUMERICAL RECIPES The Art of Scientific Computing Third Edition*. Cambridge University Press, doi:10.1017/CBO9781107415324.004
 Pritchett P. L., Strangeway R. J., 1985, *Journal of Geophysical Research*, **90**, 9650
 Qu Y., Kumar P., Zhang B., 2022, *MNRAS*, **515**, 2020
 Ravi V., et al., 2019, *Nature*, **572**, 352
 Ryder S. D., et al., 2023, *Science*, **382**, 294
 Sagiv A., Waxman E., 2002, *ApJ*, **574**, 861
 Sironi L., Plotnikov I., Näätäjä J., Beloborodov A. M., 2021, *Phys. Rev. Lett.*, **127**, 035101
 Sobacchi E., Iwamoto M., Sironi L., Piran T., 2024a, *arXiv e-prints*, p. arXiv:2409.04127
 Sobacchi E., Iwamoto M., Sironi L., Piran T., 2024b, *arXiv e-prints*, p. arXiv:2409.10732
 Stix T. H., 1992, *Waves in plasmas*. Springer Science & Business Media
 Treumann R. A., 2006, *A&ARv*, **13**, 229
 Vedenov A., Velikhov E., Sagdeev R., 1961, *Nuclear Fusion*, **1**, 82
 Wang C. B., Wu C. S., 2009, *Physics of Plasmas*, **16**, 020703
 Wang C. B., Wu C. S., Yoon P. H., 2006, *Phys. Rev. Lett.*, **96**, 125001
 Winglee R. M., Dulk G. A., 1986, *ApJ*, **310**, 432
 Wu C. S., 1985, *Space Sci. Rev.*, **41**

Wu C. S., Lee L. C., 1979, *ApJ*, **230**, 621

Wu C. S., Yoon P. H., 2007, *Phys. Rev. Lett.*, **99**, 075001

Wu D. J., Chen L., Zhao G. Q., Tang J. F., 2014, *A&A*, 566

Yoon P. H., Wang C. B., Wu C. S., 2009, *Physics of Plasmas*, **16**

Zhang B., 2020, *Nature*, 587

Zhao G. Q., Wu C. S., 2013, *Physics of Plasmas*, **20**

APPENDIX A: SEMI-ANALYTICAL EXAMINATION OF THE TERMS IN THE QUASILINEAR KINETIC EQUATION

In this section we retrieve some semi-analytical approximations for the ratios of the various terms in equation (3) in the low and intermediate magnetization regimes, specifically for $\sigma_{rel} < \sigma_1$, equivalent to $I_2/I_1 \gg 1$.

A1 Mixed term

The change in the distribution due to the mixed term, $(\frac{\partial F_0}{\partial t})_{mix}$, for an initial symmetric Maxwell-Jüttner distribution is given by

$$\begin{aligned} \left(\frac{\partial F_0}{\partial t}\right)_{mix} &= \frac{C e^{-\sqrt{1+q_{\parallel}^2+q_{\perp}^2}} q_{\parallel} q_{\perp}^2}{\theta (1+q_{\parallel}^2+q_{\perp}^2)^2} \left(1+\theta^{-1}\sqrt{1+q_{\parallel}^2+q_{\perp}^2}\right) \\ &\times \left(I_1(1+q_{\parallel}^2+q_{\perp}^2) - I_2 q_{\parallel} \sqrt{1+q_{\parallel}^2+q_{\perp}^2}\right), \end{aligned} \quad (\text{A1})$$

where C contains all the constants omitted for clarity. Fig. A1 shows the values of $|q_{\parallel,max}|$ and $|q_{\perp,max}|$ as a function of I_2/I_1 for various temperatures, showing that $|q_{\perp,max}|$ is close to constant and $|q_{\parallel,max}| \propto (I_2/I_1)^{-1}$ for large $I_2/I_1 \gg 1$ for all temperatures. It is also seen that $|q_{\parallel,max}| \ll 1$ and $|q_{\parallel,max}| \ll |q_{\perp,max}|$ in this I_2/I_1 range. Therefore comparing $(\frac{\partial F}{\partial t})_{mix,max}$ at two different values of (I_2/I_1) and $(I_2/I_1)'$ gives

$$\begin{aligned} \frac{(\frac{\partial F}{\partial t})_{mix,max}}{(\frac{\partial F}{\partial t})'_{mix,max}} &\approx \left(\frac{q_{\parallel,max}}{q'_{\parallel,max}}\right) \\ &\times \left(\frac{1+q_{\perp,max}^2 - (I_2/I_1)q_{\parallel,max}\sqrt{1+q_{\perp,max}^2}}{1+q_{\perp,max}^2 - (I_2/I_1)'q'_{\parallel,max}\sqrt{1+q_{\perp,max}^2}}\right). \end{aligned} \quad (\text{A2})$$

Defining C_{\parallel} as a constant of proportionality such that $q_{\parallel,max} = C_{\parallel}(I_2/I_1)^{-1}$, this expression can be simplified to

$$\begin{aligned} \frac{(\frac{\partial F}{\partial t})_{mix,max}}{(\frac{\partial F}{\partial t})'_{mix,max}} &\approx \frac{C_{\parallel}(I_2/I_1)'(1+q_{\perp,max}^2 - C_{\parallel}\sqrt{1+q_{\perp,max}^2})}{C_{\parallel}(I_2/I_1)(1+q_{\perp,max}^2 - C_{\parallel}\sqrt{1+q_{\perp,max}^2})} \\ &\approx \frac{(I_2/I_1)'}{(I_2/I_1)}, \end{aligned} \quad (\text{A3})$$

showing that $(\frac{\partial F}{\partial t})_{mix,max} \propto (I_2/I_1)^{-1}$ for large $I_2/I_1 \gg 1$.

A2 Parallel terms

In the case of the parallel terms, the maximum value of the parallel advection term $(\frac{\partial F_0}{\partial t})_{\parallel,1}$ is significantly higher than

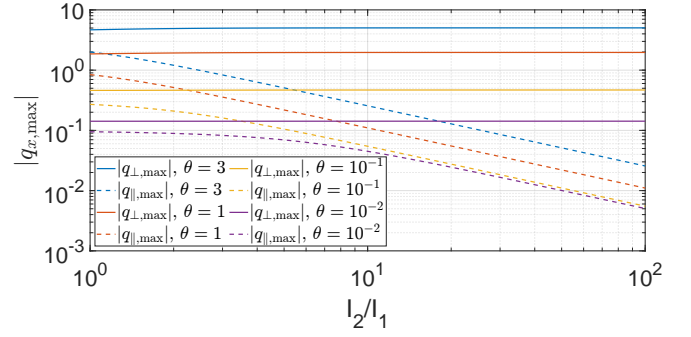


Figure A1. The values of $|q_{\parallel,max}|$ and $|q_{\perp,max}|$ as a function of I_2/I_1 for the mixed term, $(\frac{\partial F}{\partial t})_{mix}$. Dashed lines indicate $|q_{\parallel,max}|$ at different temperatures while solid lines show $|q_{\perp,max}|$. For large $I_2/I_1 \gg 1$, $|q_{\parallel,max}| \propto (I_2/I_1)^{-1}$ and $|q_{\perp,max}|$ is constant.

the diffusion term, as is shown in Fig. 8. For an initial symmetric Maxwell-Jüttner distribution, the term is

$$\begin{aligned} \left(\frac{\partial F}{\partial t}\right)_{\parallel,1} &= \frac{C e^{-\theta^{-1}\sqrt{1+q_{\parallel}^2+q_{\perp}^2}} \theta^{-1} q_{\parallel}}{(1+q_{\parallel}^2+q_{\perp}^2)} \\ &\times \left(I_1(2+2q_{\parallel}^2+3q_{\perp}^2) - 2I_2 q_{\parallel} \sqrt{1+q_{\parallel}^2+q_{\perp}^2}\right), \end{aligned} \quad (\text{A4})$$

where C contains all the constants omitted for clarity. Fig. A2 shows the values of $|q_{\parallel,max}|$ as a function of I_2/I_1 for various temperatures, while $|q_{\perp,max}| = 0$ for all cases. This allows us to discard all terms containing $q_{\perp,max}$, resulting in

$$\begin{aligned} \left(\frac{\partial F}{\partial t}\right)_{\parallel,max} &= \frac{C e^{-\theta^{-1}\sqrt{1+q_{\parallel,max}^2}} \theta^{-1} q_{\parallel,max}}{(1+q_{\parallel,max}^2)} \\ &\times \left(2I_1(1+q_{\parallel,max}^2)^2 - 2I_2 q_{\parallel,max} \sqrt{1+q_{\parallel,max}^2}\right). \end{aligned} \quad (\text{A5})$$

From Fig. A2, it is clear that $|q_{\parallel,max}|$ is close to constant for a given temperature for large I_2/I_1 . Therefore comparing $(\frac{\partial F}{\partial t})_{\parallel,max}$ at two different values of (I_2/I_1) and $(I_2/I_1)'$ gives

$$\frac{(\frac{\partial F}{\partial t})_{\parallel,max}}{(\frac{\partial F}{\partial t})'_{\parallel,max}} = \frac{(1+q_{\parallel,max}^2)^2 - (I_2/I_1)q_{\parallel,max}\sqrt{1+q_{\parallel,max}^2}}{(1+q_{\parallel,max}^2)^2 - (I_2/I_1)'q_{\parallel,max}\sqrt{1+q_{\parallel,max}^2}}. \quad (\text{A6})$$

As the ratio $\left|\frac{(1+q_{\parallel,max}^2)^2}{q_{\parallel,max}\sqrt{1+q_{\parallel,max}^2}}\right| = \gamma(q_{\parallel,max}, 0)^2/|\beta_{\parallel,max}| < 15$ for $\theta \leq 3$, the second term is always larger than the first for large values of I_2/I_1 and thus $(\frac{\partial F}{\partial t})_{\parallel,max} \propto I_2/I_1$ for $I_2/I_1 \gg 1$.

A3 Perpendicular terms

In the case of the perpendicular terms, both the advection and diffusion terms are significant, depending on the magnetization. For an initial symmetric Maxwell-Jüttner distribu-

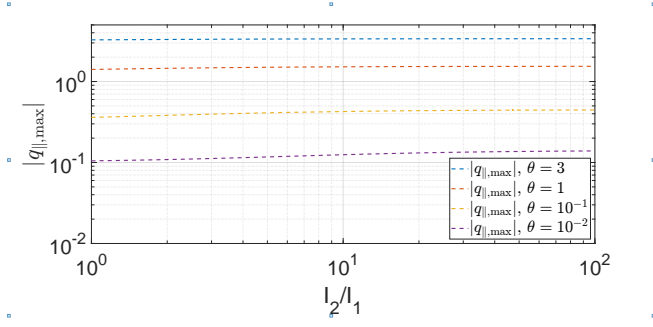


Figure A2. The values of $|q_{||,\max}|$ as a function of I_2/I_1 for the parallel advection term, $\left(\frac{\partial F}{\partial t}\right)_{||,1} \cdot |q_{\perp,\max}| = 0$ for all temperatures displayed. For large $I_2/I_1 \gg 1$, $|q_{||,\max}|$ is approximately constant.

tion, the sum of these terms is given by

$$\begin{aligned} \left(\frac{\partial F}{\partial t}\right)_{\perp} &= \frac{C e^{-\theta^{-1} \sqrt{1+q_{||}^2+q_{\perp}^2}}}{\theta^2 \gamma^4} \left\{ I_1 q_{||} \gamma^2 (-2q_{\perp}^2 \gamma + 4\theta(\gamma^2 - q_{\perp}^2)) \right. \\ &+ I_2 [\theta \gamma q_{\perp}^2 (1 + q_{\perp}^2) + q_{||}^4 (q_{\perp}^2 - 2\theta\gamma) \\ &+ q_{||}^2 (q_{\perp}^2 + q_{\perp}^4 - 2\theta\gamma)] \\ &\left. + I_3 \gamma^2 (q_{\perp}^4 - 2\theta\gamma(1 + q_{||}^2) + q_{\perp}^2 (1 + q_{||}^2 - 3\theta\gamma)) \right\}. \end{aligned} \quad (\text{A7})$$

Fig. A3 shows the values of $|q_{||,\max}|$ and $|q_{\perp,\max}|$ as a function of I_2/I_1 for various temperatures, showing that $|q_{\perp,\max}|$ is close to constant and $|q_{||,\max}| \ll 1$ and $|q_{||,\max}| \ll |q_{\perp,\max}|$ for large I_2/I_1 . We can therefore approximate $\left(\frac{\partial F}{\partial t}\right)_{\perp,\max}$ as

$$\begin{aligned} \left(\frac{\partial F}{\partial t}\right)_{\perp,\max} &\approx \frac{C e^{-\theta^{-1} \sqrt{1+q_{\perp,\max}^2}}}{\theta^2 (1 + q_{\perp,\max}^2)} \\ &\times \left\{ I_2 \theta q_{\perp,\max}^2 \right. \\ &\left. + I_3 (q_{\perp,\max}^2 \sqrt{1 + q_{\perp,\max}^2} - \theta(2 + 3q_{\perp,\max}^2)) \right\}. \end{aligned} \quad (\text{A8})$$

Now using the relation $I_3/I_1 = I_1/I_2$, which is true in the linear regime, comparing the value of $\left(\frac{\partial F}{\partial t}\right)_{\perp,\max}$ at two different values of $(I_2/I_1)'$ and (I_2/I_1) gives

$$\begin{aligned} \frac{\left(\frac{\partial F}{\partial t}\right)_{\perp,\max}}{\left(\frac{\partial F}{\partial t}\right)'_{\perp,\max}} &\approx \frac{(I_2/I_1)'}{(I_2/I_1)} \\ &\times \left(\frac{q_{\perp,\max}^2 \sqrt{1 + q_{\perp,\max}^2} + \theta(q_{\perp,\max}^2 ((I_2/I_1)^2 - 3) - 2)}{q_{\perp,\max}^2 \sqrt{1 + q_{\perp,\max}^2} + \theta(q_{\perp,\max}^2 ((I_2/I_1)'^2 - 3) - 2)} \right) \\ &\approx \frac{(I_2/I_1)'}{(I_2/I_1)} \frac{q_{\perp,\max}^2 \sqrt{1 + q_{\perp,\max}^2} + \theta q_{\perp,\max}^2 (I_2/I_1)^2}{q_{\perp,\max}^2 \sqrt{1 + q_{\perp,\max}^2} + \theta q_{\perp,\max}^2 (I_2/I_1)'^2}, \end{aligned} \quad (\text{A9})$$

which is valid for $I_2/I_1 \gg 1$. This ratio becomes

$$\frac{\left(\frac{\partial F}{\partial t}\right)_{\perp,\max}}{\left(\frac{\partial F}{\partial t}\right)'_{\perp,\max}} \approx \frac{(I_2/I_1)}{(I_2/I_1)'}, \quad (\text{A10})$$

when $\theta(I_2/I_1)^2 \gg \sqrt{1 + q_{\perp,\max}^2} = \gamma(0, q_{\perp,\max})$. As $|q_{\perp,\max}|$ increases monotonically with temperature from $|q_{\perp,\max}| \sim$

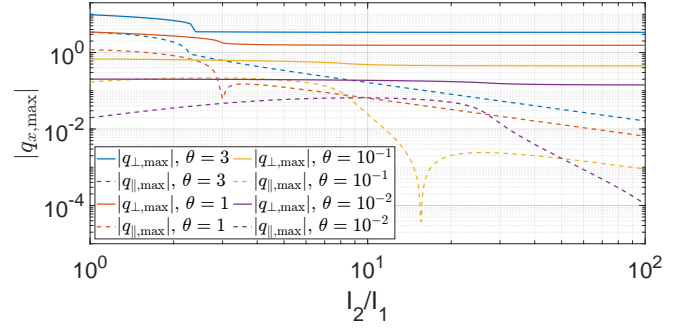


Figure A3. The values of $|q_{||,\max}|$ and $|q_{\perp,\max}|$ as a function of I_2/I_1 for the combined perpendicular terms $\left(\frac{\partial F}{\partial t}\right)_{\perp}$. Dashed lines indicate $|q_{||,\max}|$ at different temperatures while solid lines show $|q_{\perp,\max}|$. For large $I_2/I_1 \gg 1$, $|q_{||,\max}| \ll 1$ and $|q_{\perp,\max}|$ is approximately constant. The sharp dips in $|q_{||,\max}|$ are due to a change in sign.

0.14 for $\theta = 10^{-2}$ to $|q_{\perp,\max}| \sim 3.4$ for $\theta = 3$, this condition is satisfied in the $I_2/I_1 \gg 1$ regime, confirming that $\left(\frac{\partial F}{\partial t}\right)_{\perp,\max} \propto I_2/I_1$ for low magnetizations.

This paper has been typeset from a $\text{\TeX}/\text{\LaTeX}$ file prepared by the author.